International Journal of Mechanical System Dynamics

WILEY

IJMSD International Journal of Mechanical System Dynamics Open Access

RESEARCH ARTICLE OPEN ACCESS

Effect of Orthotropic Variable Foundations and Unconventional Support Conditions on Nonlinear Hygrothermoelectric Vibration of Porous Multidirectional Piezoelectric Functionally Graded Nonuniform Plate

Pawan Kumar[1] | Sontipee Aimmanee[1] | Suraj Prakash Harsha[2]

[1]Advanced Materials and Structures Laboratory (AMASS), Faculty of Engineering, King Mongkut's University of Technology Thonburi, Bangkok, Thailand | [2]Advanced Mechanical Vibration Lab, Mechanical & Industrial Engineering Department, IIT Roorkee, Roorkee, India

Correspondence: Pawan Kumar (pawan4770@gmail.com) | Sontipee Aimmanee (sontipee.aim@kmutt.ac.th)

Received: 13 January 2025 | **Revised:** 16 March 2025 | **Accepted:** 19 March 2025

Funding: This study was supported by King Mongkut's University of Technology Thonburi's Postdoctoral Fellowship Under Research Project ID- 27929

Keywords: conventional and unconventional support conditions | hygrothermal loading | multidirectional material exponent | orthotropic angle | tapered ratio | variable elastic foundation

ABSTRACT

This article investigates the nonlinear vibration behavior of porous multidirectional piezoelectric functionally graded nonuniform (PFGN) plates resting on orthotropic variable elastic foundations and subjected to hygrothermal loading. The sigmoidal law is employed to define the multidirectional gradation properties, incorporating porosity along both the axial and thickness directions. The governing equations for the porous multidirectional PFGN plate are derived using the modified first-order shear deformation theory (FSDT) with nonlinear von Kármán strain and Hamilton's principle. A higher-order finite element (FE) approach, combined with a modified Newton-Raphson method, is utilized to solve the resulting equations. The study reveals that orthotropic variable elastic foundations significantly influence the vibration behavior of multidirectional PFGN porous plates compared to conventional elastic foundations under hygrothermal loading. Additionally, the effects of various parameters such as thickness ratio, tapered ratio, material exponent, boundary conditions, porosity distribution, electrical loading, temperature variation, and moisture change on the vibration behavior are comprehensively analyzed. The results of this study have direct applications in energy harvesting and structural health monitoring, offering a novel approach to designing and optimizing smart materials for engineering systems operating under hygrothermal and thermoelectrical conditions.

1 | Introduction

Piezoelectric materials are widely used in innovative structures and systems owing to their inherent electromechanical behavior [1]. Traditional piezoelectric devices, which are bonded with piezoelectric actuators and sensors, are commonly referred to as smart structures [2]. However, these devices exhibit some limitations, such as delamination, cracking, and high-stress concentrations at the interfaces between layers. Functionally graded materials (FGMs) are a new class of composite materials that offer a promising solution to address these issues and, therefore, they are applied to a wide range of real-world applications [3]. When FGMs [4, 5] are combined with piezoelectric materials, they form functionally graded piezoelectric

---

(FGP) materials [6, 7]. FGMs are heterogeneous materials created by combining two or more metals or alloys, resulting in a gradual variation in the material phases [8, 9]. It has been both experimentally and theoretically proven that the gradation properties of FGMs can significantly enhance the stability, consistency, and performance of piezoelectric structures [10, 11].

Several studies have explored the behavior of functionally graded plates and materials under various conditions, Zhong and Shang [12] conducted a 3D exact analysis of a simply supported FGP material plate, and the final equations are developed based on the state space approach. Uymaz and Aydogdu [13] presented the 3D vibrational response of the rectangular FG plate with boundary conditions using the elasticity theory. Huang and Shen [14] investigated the FG plates' nonlinear dynamic and vibration behavior under thermal environments using HSDT. Manna [15] studied the vibration responses of an isotropic tapered rectangular plate using triangular elements and FSDT. Behjat and Khoshravan [16] examined the free vibration and static behavior of FG piezoelectric plates subjected to various electromechanical loadings using the finite element method. Ramteke et al. [17] analyzed the eigen behavior of the multidirectional FG porous panels under thermomechanical loading using the FE techniques. Kumar and Harsha [18] presented the electromechanical static and vibrational responses of sigmoid-based FG smart plates using FSDT and higher-order finite element formulations. Xiang and Shi [19] investigated the static behavior of the FG piezoelectric plate as actuators and sensors subjected to the thermal and electromechanical loads. Komeili et al. [20] examined the static bending of the FG piezoelectric beams subjected to thermoelectric loading using finite element formulations with Hamilton's principle.

Pores or voids can form within materials during FG materials' fabrication or manufacturing process. These imperfections can be detrimental to the performance of high-performance composites, leading to decreasing efficiency and material failures. As a result, this issue has attracted considerable research attention. For example, Barati and Zenkour [21] presented the thermoelectric vibration response of the piezoelectric FG porous plate with several boundary conditions. Kumar and Harsha [22–24] examined the vibration and dynamic behavior of the piezoelectric FG porous plate [25] subjected to different thermoelectric loading using FE formulations. Şimşek [26] investigated the dynamic vibration of the bidirectional graded beams. Lü et al. [27] studied the vibration response of the thick, simply supported FG plate resting on foundations. Chen et al. [28] explored the free, forced, and static behavior of shear deformable FG porous beams. Van Vinh et al. [29] conducted a static analysis of graded plates using C0 four-node quadrilateral element-based FE techniques. Nan et al. [30] analyzed the static bending and free vibration behavior of FG piezoelectric beams with size-dependent porosity. Zhao et al. [31] examined the effects of flexoelectricity and porosity on the axial free vibration and static behavior of FG piezoelectric beams. Rad [32] examined the static behavior of the tapered auxetic FG porous circular plates using the quadrature method. Li et al. [33] studied the bidirectional porous FG plates' vibration and buckling responses using the FSDT and isogeometric analysis.

Numerous analytical and numerical approaches have been employed to study the thermomechanical responses of FG plates, beams, and shells resting on various elastic foundations [34]. For instance, Mudhaffar et al. [35] examined the bending responses of FG plates subjected to hygrothermal loads while resting on viscoelastic foundations. Prakash et al. [36] investigated the thermoelastic response of FG plates with elastic foundations using isogeometric analysis. Kumar and Harsha [37, 38] explored the effects of different elastic foundations—such as Winkler, Pasternak, and Kerr foundations—on piezoelectric graded plates subjected to thermoelectrical loading. Tornabene [39] studied the free vibration behavior of FG-based structures, including shells and annular plates with power law distributions.

Additionally, there has been limited research on the vibration behavior of FG plates with orthotropic variable foundations. Elastic foundations play a crucial role in various structural engineering applications, such as reinforced concrete pavements, highways and airport runways, storage tank foundations, swimming pools, deep walls, and building foundation slabs. One commonly used model to represent these foundations is Winkler's elastic foundation, which assumes that the underlying layers consist of independent, unconnected springs. However, a significant limitation of this model is the lack of interaction between individual springs. To address this, the Pasternak foundation model, a two-parameter model that incorporates the foundation's shear stiffness, provides a more comprehensive approach compared to the Winkler foundation model [40]. From an engineering perspective, the Pasternak model offers valuable generalizations, especially when calculating interfacial stresses between structural elements and continua under elastic foundation assumptions. Given that mechanical foundations have not been typically used to interact with FG structures, the orthotropy [41] of the foundation and soil continuum is a recognized phenomenon. Several studies have addressed this area. For instance, Arani et al. [42] examined the vibration behavior of a nanoplate resting on orthotropic Pasternak foundations. Sharif et al. [43] investigated the effect of a hygrothermal environment on the free vibration behavior of a nano sandwich plate resting on orthotropic Pasternak foundations. Ermis et al. [44] presented the vibration behavior of an FG beam resting on orthotropic Pasternak foundations using mixed finite element formulations.

Furthermore, recent research has focused on the combined effects of several parameters, especially hybrid materials, size-dependent behaviors, and metamaterials. Li et al. [45] investigated the free vibration responses of the FG sandwich plates under the effect of the thermal environment. Karami et al. [46] studied the vibration behavior of the size-dependent, doubly curved, porous, shear-deformable FG material-based microshells. Eghbali and Hosseini [47] examined the dynamic response of the sandwich graphene-reinforced aluminum-based composite beams resting on elastic foundations. Harsha and Kumar [48, 49] studied the impact of porosity and elastic foundation on bidirectional FG piezoelectric porous plate subjected to the thermoelectrical effects. Salari et al. [50] investigated the nonlinear thermal stability and buckling response of the temperature-dependent imperfect FG nanobeams resting on elastic foundations. Kumar and Harsha [51, 52] studied the static bending, vibration, and buckling responses of the sandwich and FG piezoelectric porous plates under thermomechanical loading. Salari and Vanini [53, 54] investigated the static and dynamic response of the temperature-dependent nanoFG circular porous plate under thermal loading. Ashoori et al. [55] studied the size-dependent axisymmetric vibration behavior of FG circular plates. Kumar and Harsha [56–58] analyzed the static bending and vibration responses of the PZT-4/PZT-5H-based FG porous plates resting on elastic foundations, subjected to thermal and electrical loading. Ghadiri et al. [59] studied the thermoelectric vibration analysis of embedded single-walled boron nitride nanotubes based on nonlocal third-order beam theory. Salari et al. [60] explored the nonlinear dynamic vibration and buckling responses of FG porous nanobeams using nonlocal theory. Ebrahimi and Salari [61–63] examined the vibration responses of FG porous and FG piezoelectric plates/beams with various boundary conditions using analytical and semi-analytical methods. Kumar and Harsha [64, 65] analyzed hygrothermal effects, static bending, and vibration responses, showing that elastic foundations enhance stiffness, while material gradation influences frequencies. Ezzati et al. [66] highlighted graphene-based metamaterials for enhanced strength-to-weight ratios. Ghasemi et al. [67, 68] explored nonlinear instability in 3D-printed auxetic metastructures, integrating machine learning to improve post-buckling predictions. Previous research has established the effectiveness of orthotropic Pasternak foundations, and several other authors have studied the static and vibration responses of the FG thick/thin porous piezoelectric plates [69, 70] and metasturctures [71, 72] under thermomechanical loading.

After thoroughly reviewing the research on the vibration behavior of functionally graded (FG) structures resting on elastic foundations, the following conclusions can be drawn: Most existing studies focus on graded plates resting on elastic foundations subjected to thermomechanical loading. However, very little research has explored the nonlinear vibration behavior of multidirectional functionally graded piezoelectric (FGP) uniform/nonuniform plates resting on orthotropic variable elastic foundations with both conventional and unconventional boundary conditions.

Building on these insights, the primary objective of this study is to investigate the nonlinear vibration behavior of multidirectional piezoelectric functionally graded nonuniform (PFGN) porous plates under hygro-thermo-electromechanical loading conditions, with both conventional (CSC) and unconventional support conditions (USC). The material distribution and porosity models of multidirectional PFGN plates are described using the sigmoidal law. The final equation for the PFGN porous plate is derived using Hamilton's principle, incorporating first-order shear deformation theory (FSDT) with von Kármán nonlinear strains. This is then solved using a higher-order finite element technique coupled with a modified Newton-Raphson method. Convergence and validation of the analyses have been performed to ensure the efficacy of the methods used. The study explores the effects of several parameters, including thickness, tapered ratio, material exponent, conventional (CSC) and unconventional support conditions (USC), porosity distributions, orthotropic variable elastic foundations, electrical loading, temperature changes, and moisture variation on the vibration behavior of multidirectional PFGN porous plates.

Thus, the key novelties of this study are as follows:

- *Orthotropic variable foundations*—Unlike conventional elastic foundations, this study includes varying orthotropic elastic foundations, providing a more realistic representation of structures resting on elastic supports.
- *Unconventional support conditions*—This study incorporates unconventional support conditions alongside conventional boundary conditions, which are often encountered in complex structural systems but remain underexplored in nonlinear hygrothermoelectric vibration analyses.
- *Multidirectional material distributions*—Instead of using a simple power-law grading, this study adopts a sigmoidal material distribution model in multiple directions, which better capture real-world material behavior in high-performance applications.
- *Hygrothermoelectric effects*—Most existing studies focus only on mechanical and thermomechanical vibrations, but in real applications, humidity, temperature variations, and electric loading play a crucial role, especially in FG-graded piezoelectric materials. This study accounts for these effects, providing a more comprehensive and accurate structural response analysis.

2 | Mathematical Formulation

2.1 | Material Distribution

Consider a three-dimensional rectangular plate (as shown in Figure 1) of width a and thickness h, where both uniform (Plate A) and nonuniform (Plate B) configurations are considered in this analysis. These plates are assumed to be composed of two different piezoelectric materials, with the constituents graded in the axial y-direction and thickness z-direction. The material properties at any location in the plate's volume are defined in terms of the volume fractions V_{p4} for PZT-4 and V_{p5} for PZT-5H such that $V_{p4} + V_{p5} = 1$.

The thermomechanical properties of the porous plate vary according to sigmoid (Sg) distributions in both plate configurations. The material property distribution of the multidirectional PFGN plate, calculated based on the rule of mixture, is given by Equation (1) and visually illustrated in Figure 2 for the perfect plate (PP), even plate (EP), uneven plate (UP), and symmetric center plate (SCP):

$$\left.\begin{array}{l}\text{PP:}\quad \mathfrak{R}_{eff.} = \mathfrak{R}_{p5} + (\mathfrak{R}_{p4} - \mathfrak{R}_{p5})V_{p4}\\ \text{EP: } \mathfrak{R}_{eff.} = \mathfrak{R}_{p5} + (\mathfrak{R}_{p4} - \mathfrak{R}_{p5})V_{p4} - 0.5\Upsilon(\mathfrak{R}_{p4} + \mathfrak{R}_{p5})\\ \text{UP: } \mathfrak{R}_{eff.} = \mathfrak{R}_{p5} + (\mathfrak{R}_{p4} - \mathfrak{R}_{p5})V_{p4} - 0.5\Upsilon(\mathfrak{R}_{p4} + \mathfrak{R}_{p5})\left(1 - \frac{2\,|\,z|}{h(y)}\right)\\ \text{SCP: } \mathfrak{R}_{eff.} = \mathfrak{R}_{p5} + (\mathfrak{R}_{p4} - \mathfrak{R}_{p5})V_{p4} - \Upsilon\,\cos\left(\frac{\pi z}{h(y)}\right)\{\mathfrak{R}_{p5} + (\mathfrak{R}_{p4} - \mathfrak{R}_{p5})V_{p4}\}\end{array}\right\}, \tag{1}$$

where $\mathfrak{R}_{eff.}$ denotes a generic material property (e.g., elastic, piezoelectric and dielectric constants) of the multidirectional FGP plate, and Υ is the porous parameter [22].

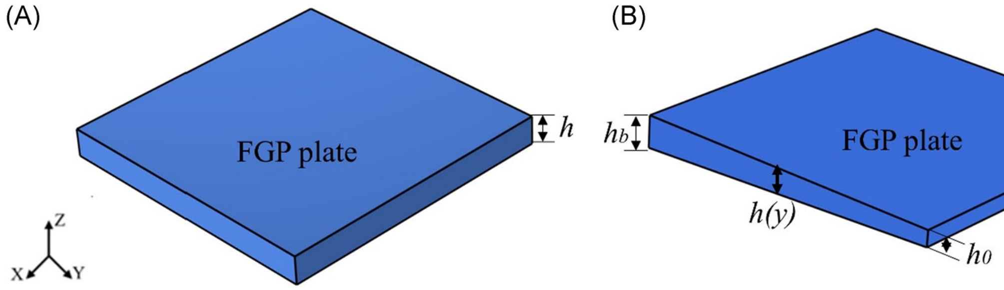

FIGURE 1 | Configurations of different FGP plates: (A) Plate A, and (B) Plate B.

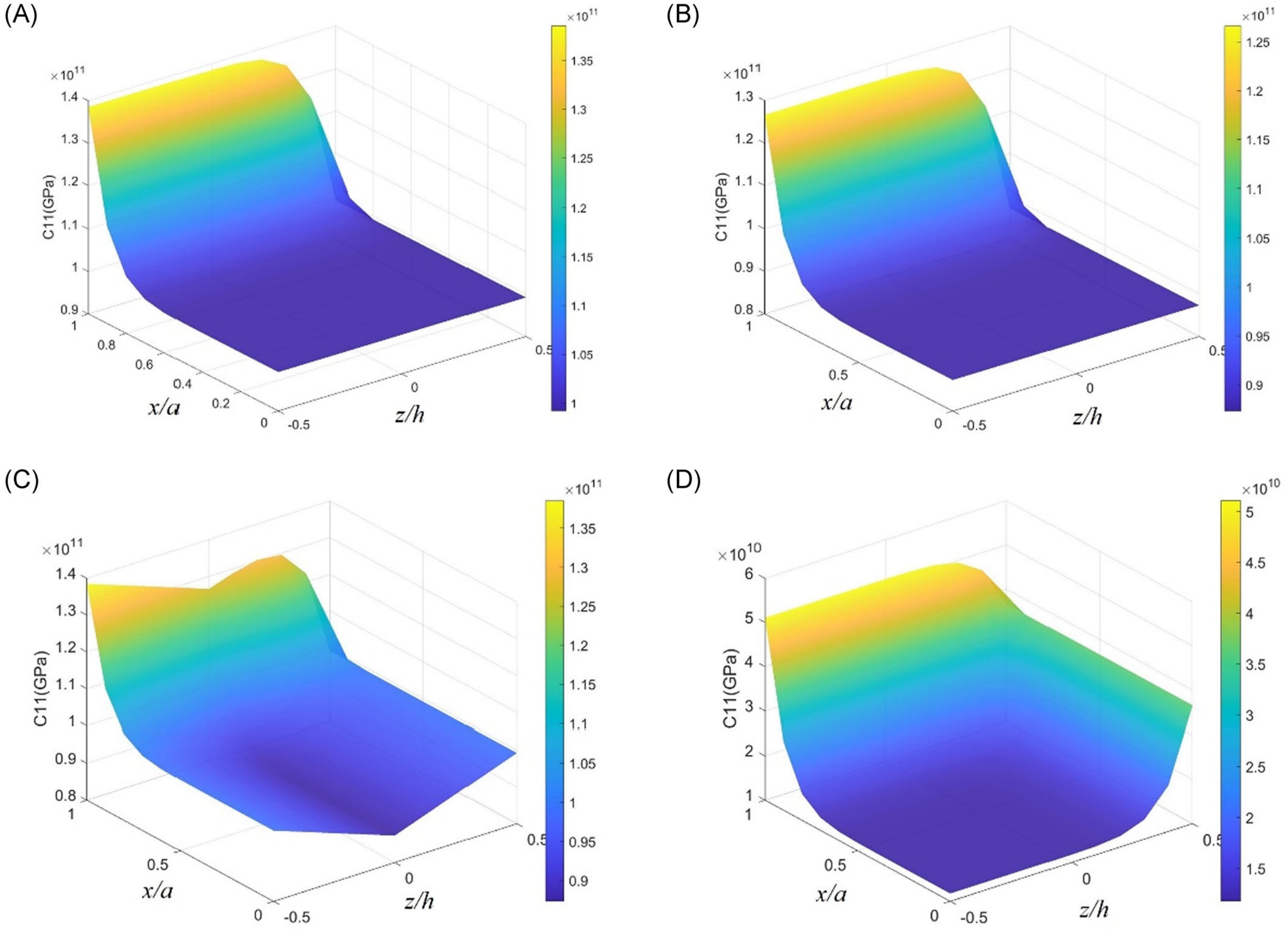

FIGURE 2 | Variations of material distributions for bidirectional porosity distributions and sigmoid (Sg) distributions: (A) PP, (B) EP, (C) UP, and (D) SCP.

- For uniform FGP plates (Plate A), the volume fraction distributions are given as:

$$V_{p4} = \begin{cases} \left[1 - 0.5\left(1 - \frac{2z}{h}\right)^{n_z}\left(\frac{x}{a}\right)^{n_x}\right];\ 0 \le z \le h/2; \\ \left[\frac{1}{2}\left(1 + \frac{2z}{h}\right)^{n_z}\left(\frac{x}{a}\right)^{n_x}\right];\ -h/2 \le z \le 0; \end{cases} \tag{2}$$

- For nonuniform FGP plates (Plate B), the volume fraction distributions are given as:

$$V_{p4} = \begin{cases} \left[1 - 0.5\left(1 - \frac{2z}{h(y)}\right)^{n_z}\left(\frac{x}{a}\right)^{n_x}\right];\ 0 \le z \le h(y)/2; \\ \left[\frac{1}{2}\left(1 + \frac{2z}{h(y)}\right)^{n_z}\left(\frac{x}{a}\right)^{n_x}\right];\ -h(y)/2 \le z \le 0; \end{cases} \tag{3}$$

The variable thickness parameter distribution in the y-direction is considered as:

$$h(y) = h_0\left(1 + \beta_{tr}\left(\frac{y}{a}\right)\right);\ \beta_{tr} = \frac{h_b - h_0}{h_0}; \tag{4}$$

where β_{tr} is the varying thickness ratio, h_b is the initial thickness of the plate, and h_0 is the final thickness. The dimensionless parameter (y/a) is used along with the power law exponents n_x, and n_z denoting the thickness variation in the x- and z-directions, respectively.

2.2 | Constitutive Equations

The stress-stain constitutive relation for the hygro-thermoelectroelastic medium of the multidirectional PFGN plates is expressed as follows [35, 37, 73]:

$$\begin{aligned} \{\boldsymbol{\sigma}\} &= [\boldsymbol{C}](\{\boldsymbol{\varepsilon}\} - [\boldsymbol{\alpha}]\Delta T - [\boldsymbol{\beta}]\Delta M) - [\boldsymbol{e}]\{\boldsymbol{E}\}; \\ \{\boldsymbol{D}\} &= [\boldsymbol{e}]^{\mathrm{T}}(\{\boldsymbol{\varepsilon}\} - [\boldsymbol{\alpha}]\Delta T - [\boldsymbol{\beta}]\Delta M) + [\boldsymbol{\kappa}]\{\boldsymbol{E}\}; \end{aligned} \tag{5}$$

where $\{\boldsymbol{\sigma}\}$, $\{\boldsymbol{D}\}$, $\{\boldsymbol{\varepsilon}\}$, and $\{\boldsymbol{E}\}$ are components of the stress field, electric displacement, strain, and electric field, respectively; $\Delta T = T - T_{\mathrm{ref}}$ is the temperature change, with T and T_{ref} denoting the temperature field and reference temperature, respectively; $\Delta M = M - M_{\mathrm{ref}}$ represents the moisture change, with M and M_{ref} indicating the applied moisture field and reference moisture concentration, respectively; and $[\boldsymbol{C}]$, $[\boldsymbol{e}]$, and $[\boldsymbol{\kappa}]$ are the elastic, piezoelectric, and dielectric constants, respectively. The properties $[\boldsymbol{\alpha}]$ and $[\boldsymbol{\beta}]$ correspond to the coefficients of thermal expansion and moisture concentration, respectively.

The detailed form of Equation (5) under the plane stress state, combined with the transverse shear stresses, can be expressed as follows [73, 74]:

$$\begin{Bmatrix} \sigma_{11} \\ \sigma_{22} \\ \tau_{12} \\ \tau_{13} \\ \tau_{23} \end{Bmatrix} = \begin{bmatrix} \overline{C}_{11} & \overline{C}_{12} & 0 & 0 & 0 \\ \overline{C}_{12} & \overline{C}_{22} & 0 & 0 & 0 \\ 0 & 0 & \overline{C}_{66} & 0 & 0 \\ 0 & 0 & 0 & \overline{C}_{44} & 0 \\ 0 & 0 & 0 & 0 & \overline{C}_{55} \end{bmatrix} \left(\begin{Bmatrix} \varepsilon_{11} \\ \varepsilon_{22} \\ \gamma_{12} \\ \gamma_{13} \\ \gamma_{23} \end{Bmatrix} - \begin{Bmatrix} \overline{\alpha}_1 \\ \overline{\alpha}_2 \\ 0 \\ 0 \\ 0 \end{Bmatrix} \Delta T - \begin{Bmatrix} \overline{\beta}_1 \\ \overline{\beta}_2 \\ 0 \\ 0 \\ 0 \end{Bmatrix} \Delta M \right) - \begin{bmatrix} 0 & 0 & \bar{e}_{31} \\ 0 & 0 & \bar{e}_{32} \\ 0 & 0 & 0 \\ 0 & \bar{e}_{24} & 0 \\ \bar{e}_{15} & 0 & 0 \end{bmatrix} \begin{Bmatrix} E_1 \\ E_2 \\ E_3 \end{Bmatrix}; \tag{6}$$

$$\begin{Bmatrix} D_1 \\ D_2 \\ D_3 \end{Bmatrix} = \begin{bmatrix} 0 & 0 & 0 & 0 & \bar{e}_{15} \\ 0 & 0 & 0 & \bar{e}_{24} & 0 \\ \bar{e}_{31} & \bar{e}_{32} & 0 & 0 & 0 \end{bmatrix} \left(\begin{Bmatrix} \varepsilon_{11} \\ \varepsilon_{22} \\ \gamma_{12} \\ \gamma_{13} \\ \gamma_{23} \end{Bmatrix} - \begin{Bmatrix} \overline{\alpha}_1 \\ \overline{\alpha}_2 \\ 0 \\ 0 \\ 0 \end{Bmatrix} \Delta T - \begin{Bmatrix} \overline{\beta}_1 \\ \overline{\beta}_2 \\ 0 \\ 0 \\ 0 \end{Bmatrix} \Delta M \right) + \begin{bmatrix} \overline{\kappa}_{11} & 0 & 0 \\ 0 & \overline{\kappa}_{22} & 0 \\ 0 & 0 & \overline{\kappa}_{33} \end{bmatrix} \begin{Bmatrix} E_1 \\ E_2 \\ E_3 \end{Bmatrix}; \tag{7}$$

where $[\overline{\boldsymbol{C}}]$, $[\bar{\boldsymbol{e}}]$, $[\overline{\boldsymbol{\kappa}}]$, $[\overline{\boldsymbol{\alpha}}]$, and $[\overline{\boldsymbol{\beta}}]$ are the reduced elastic constants, reduced piezoelectric constants, reduced dielectric constants, and the reduced coefficients of thermal expansion and moisture concentration, respectively. These material properties can be derived as follows:

$$\left.\begin{aligned} &\overline{C}_{11} = C_{11} - \frac{C_{13}^2}{C_{33}}, \overline{C}_{12} = C_{12} - \frac{C_{13}C_{23}}{C_{33}}, \overline{C}_{22} = C_{22} - \frac{C_{23}^2}{C_{33}}, \overline{C}_{44} = C_{44}, \\ &\overline{C}_{55} = C_{55}, \overline{C}_{66} = C_{66}, \bar{e}_{24} = e_{24}, \bar{e}_{15} = e_{15}, \bar{e}_{31} = e_{31} - \frac{C_{13}e_{33}}{C_{33}}, \\ &\bar{e}_{32} = e_{32} - \frac{C_{23}e_{33}}{C_{33}}, \overline{\kappa}_{11} = \kappa_{11}, \overline{\kappa}_{22} = \kappa_{22}, \overline{\kappa}_{33} = \kappa_{33} + \frac{e_{23}^2}{C_{33}}, \\ &\overline{\alpha}_1 = \alpha_1 - \frac{C_{13}\alpha_3}{C_{33}}, \overline{\alpha}_{22} = \alpha_2 - \frac{C_{13}\alpha_3}{C_{33}}, \overline{\beta}_1 = \beta_1 - \frac{C_{13}\beta_3}{C_{33}}, \overline{\beta}_2 = \beta_2 - \frac{C_{13}\beta_3}{C_{33}}, \end{aligned}\right\}. \tag{8}$$

To facilitate the formulation presented below, the matrices and vectors appearing in Equations (5–7) can be subdivided based on the bending and shear parts as

$$\left.\begin{aligned} &[\boldsymbol{\sigma}_{bp}] = \begin{Bmatrix} \sigma_{11} \\ \sigma_{22} \\ \tau_{12} \end{Bmatrix}; [\boldsymbol{\sigma}_{sp}] = \begin{Bmatrix} \tau_{13} \\ \tau_{23} \end{Bmatrix}; [\boldsymbol{\varepsilon}_{bp}] = \begin{Bmatrix} \varepsilon_{11} \\ \varepsilon_{22} \\ \gamma_{12} \end{Bmatrix}; [\boldsymbol{\varepsilon}_{sp}] = \begin{Bmatrix} \gamma_{13} \\ \gamma_{23} \end{Bmatrix}; [\boldsymbol{C}_{bp}] = \begin{bmatrix} \overline{C}_{11} & \overline{C}_{12} & 0 \\ \overline{C}_{12} & \overline{C}_{22} & 0 \\ 0 & 0 & \overline{C}_{66} \end{bmatrix}; [\boldsymbol{C}_{sp}] = \begin{bmatrix} \overline{C}_{44} & 0 \\ 0 & \overline{C}_{55} \end{bmatrix}; \\ &[\boldsymbol{e}_{bp}] = \begin{bmatrix} 0 & 0 & \bar{e}_{31} \\ 0 & 0 & \bar{e}_{32} \\ 0 & 0 & 0 \end{bmatrix}; [\boldsymbol{e}_{sp}] = \begin{bmatrix} 0 & \bar{e}_{24} & 0 \\ \bar{e}_{15} & 0 & 0 \end{bmatrix}; [\boldsymbol{\kappa}] = \begin{bmatrix} \overline{\kappa}_{11} & 0 & 0 \\ 0 & \overline{\kappa}_{22} & 0 \\ 0 & 0 & \overline{\kappa}_{33} \end{bmatrix}; [\boldsymbol{\alpha}] = \begin{Bmatrix} \overline{\alpha}_1 \\ \overline{\alpha}_2 \\ 0 \\ 0 \\ 0 \end{Bmatrix}; [\boldsymbol{\beta}] = \begin{Bmatrix} \overline{\beta}_1 \\ \overline{\beta}_2 \\ 0 \\ 0 \\ 0 \end{Bmatrix}. \end{aligned}\right\} \tag{9}$$

Following the framework of FSDT, the displacement field of the multidirectional PFGN plate, whose components are denoted by u_i, can be stated as follows [74]:

$$\begin{aligned} u_1 = u_0(x, y, t) + z\varphi_1(x, y, t); u_2 = v_0(x, y, t) \\ + z\varphi_2(x, y, t); u_3 = w_0(x, y, t), \end{aligned} \tag{10}$$

where u_0, v_0, and w_0 are the mid-plane displacement in the x-, y-, and z-directions, respectively. These displacements can be written in a vector form as $\{\boldsymbol{u}_t\}$. The bending rotations about the y and x-axes are denoted by φ_1 and φ_2, respectively, which can be written in a vector form as $\{\boldsymbol{u}_r\}$.

Using von Kármán theory of geometrically nonlinear strains, the displacement field leads to the following displacement-strain relations:

$$\left.\begin{array}{l}\varepsilon_{11}=\frac{\partial u_0}{\partial x}+\frac{1}{2}\left(\frac{\partial w_0}{\partial x}\right)^2+z\frac{\partial\varphi_1}{\partial x};\ \varepsilon_{22}=\frac{\partial v_0}{\partial y}+\frac{1}{2}\left(\frac{\partial w_0}{\partial y}\right)^2+z\frac{\partial\varphi_2}{\partial y};\\ \gamma_{12}=\frac{\partial u_0}{\partial y}+\frac{\partial v_0}{\partial x}+\left(\frac{\partial w_0}{\partial x}\frac{\partial w_0}{\partial y}\right)+z\frac{\partial\varphi_1}{\partial x}+z\frac{\partial\varphi_2}{\partial y};\\ \gamma_{13}=\frac{\partial w_0}{\partial x}+\varphi_1;\ \gamma_{23}=\frac{\partial w_0}{\partial y}+\varphi_2;\end{array}\right\}. \tag{11}$$

The strain vectors describing the state of in-plane and transversely normal strains at any point in the multidirectional PFGN plate can be expressed as:

$$\{\varepsilon\}=\{\varepsilon_{lr}\}+\{\varepsilon_{nlr}\}, \tag{12}$$

where

$$\left.\begin{array}{l}\{\varepsilon_{lr}\}=\{\varepsilon_{bplr}\};\ \{\varepsilon_{nlr}\}=\{\varepsilon_{bpnlr}\};\ \{\varepsilon_{bp}\}=\{\varepsilon_{bplr}\}+\{\varepsilon_{bpnlr}\}\\ \{\varepsilon_{bplr}\}=[\boldsymbol{B}_1]\{\boldsymbol{u}_t\}+[\boldsymbol{z}_1][\boldsymbol{B}_2]\{\boldsymbol{u}_r\};\ \{\varepsilon_{bpnlr}\}=\frac{1}{2}[\boldsymbol{B}_3][\boldsymbol{B}_4]\{\boldsymbol{u}_t\};\\ [\varepsilon_{sp}]=[\boldsymbol{B}_5]\{\boldsymbol{u}_t\}+[\boldsymbol{z}_3][\boldsymbol{B}_6]\{\boldsymbol{u}_r\}\end{array}\right\}, \tag{13}$$

where $\{\varepsilon_{bplr}\}$ and $\{\varepsilon_{bpnlr}\}$ refer to the linear and nonlinear bending strains. $[\boldsymbol{z}_1]$ and $[\boldsymbol{z}_3]$ are the transformation matrices.

Considering the direct and converse effects of piezoelectricity, the electric potential field Θ is assumed to satisfy the Maxwell equation in the following form [10, 21]:

$$\Theta(x,y,z,t)=\frac{2z}{h(y)}V-\cos\left(\frac{\pi z}{h(y)}\right)\Theta_0(x,y,t), \tag{14}$$

where $\boldsymbol{\Theta}_0(x,y,t)$ is a function of the electric potential in the in-plane coordinates x and y, and V is the external applied voltage. The electric field E is related to the electric potential $\boldsymbol{\Theta}$ by:

$$\begin{aligned}\{\boldsymbol{E}\}&=\{E_1,E_2,E_3\}^{\mathrm{T}}=-\{(\partial\Theta/\partial x),(\partial\Theta/\partial y),(\partial\Theta/\partial z)\}^{\mathrm{T}}\\&=-[\boldsymbol{B}_\Theta]\left\{\boldsymbol{\Theta}_0^e\right\},\end{aligned} \tag{15}$$

where $\{\boldsymbol{\Theta}_0^e\}$ is the nodal electric potential vector, and the details of the $[\boldsymbol{B}]$ matrices in Equations (13) and (15) are provided in Appendix.

2.3 | Hygrothermal Loading

For the hygrothermal vibration problem, four different distributions of hygrothermal loading [42, 75] in the transverse direction of the multidirectional PFGN plate are considered, as described below.

2.3.1 | Uniform Hygrothermal Rise (UHT)

In this case, the hygrothermal rise undergoes uniform variation across the plate thickness. Specifically, the temperature and moisture concentration are given as follows:

$$T(z)=T_{fn},\ M(z)=M_{fn}, \tag{16}$$

where T_{fn} and M_{fn} are the constant final temperature and moisture concentration, respectively.

2.3.2 | Linear Hygrothermal Rise (LHT)

In this case, the hygrothermal rise assumes the linear variation across the plate thickness. The temperature and moisture concentration are given as:

$$\left.\begin{array}{l}T(y,z)=T_{p5}+(T_{p4}-T_{p5})\left(\frac{z}{h(y)}+0.5\right)\\ M(y,z)=M_{p5}+(M_{p4}-M_{p5})\left(\frac{z}{h(y)}+0.5\right)\end{array}\right\}, \tag{17}$$

where T_{p4}, T_{p5} and M_{p4}, M_{p5} are the temperature and moisture concentration at the top and bottom of the plate, respectively.

2.3.3 | Nonlinear Hygrothermal Rise (NHT)

The temperature and moisture concentration for this particular case are expressed as:

$$\left.\begin{array}{l}T(y,z)=T_{p5}+(T_{p4}-T_{p5})\left(\frac{z}{h(y)}+0.5\right)^p\\ M(y,z)=M_{p5}+(M_{p4}-M_{p5})\left(\frac{z}{h(y)}+0.5\right)^p\end{array}\right\}, \tag{18}$$

where p denotes the hygrothermal exponent, which has a value within the range $0<p<\infty, p\neq 1$. $p=3$ is considered in the present study.

3 | Variable Orthotropic Pasternak Foundation (VOPF)

Recently, various authors have examined different configurations of plate structures resting on elastic foundations, broadly adopted for modeling various engineering problems. The Well-known elastic foundation models in the literature include Winkler, Pasternak, and Kerr foundations. However, this study considers the multidirectional PFGN plate resting on different VOPFs. The orthotropic Pasternak foundation (OPF), shown in Figure 3, has an additional equivalent shear layer compared to the Winkler foundations, allowing it to resist both transverse and normal loads. Also, the stiffness of the Pasternak foundation may fluctuate orthotropically due to the random orientation of the microstructure in the foundation.

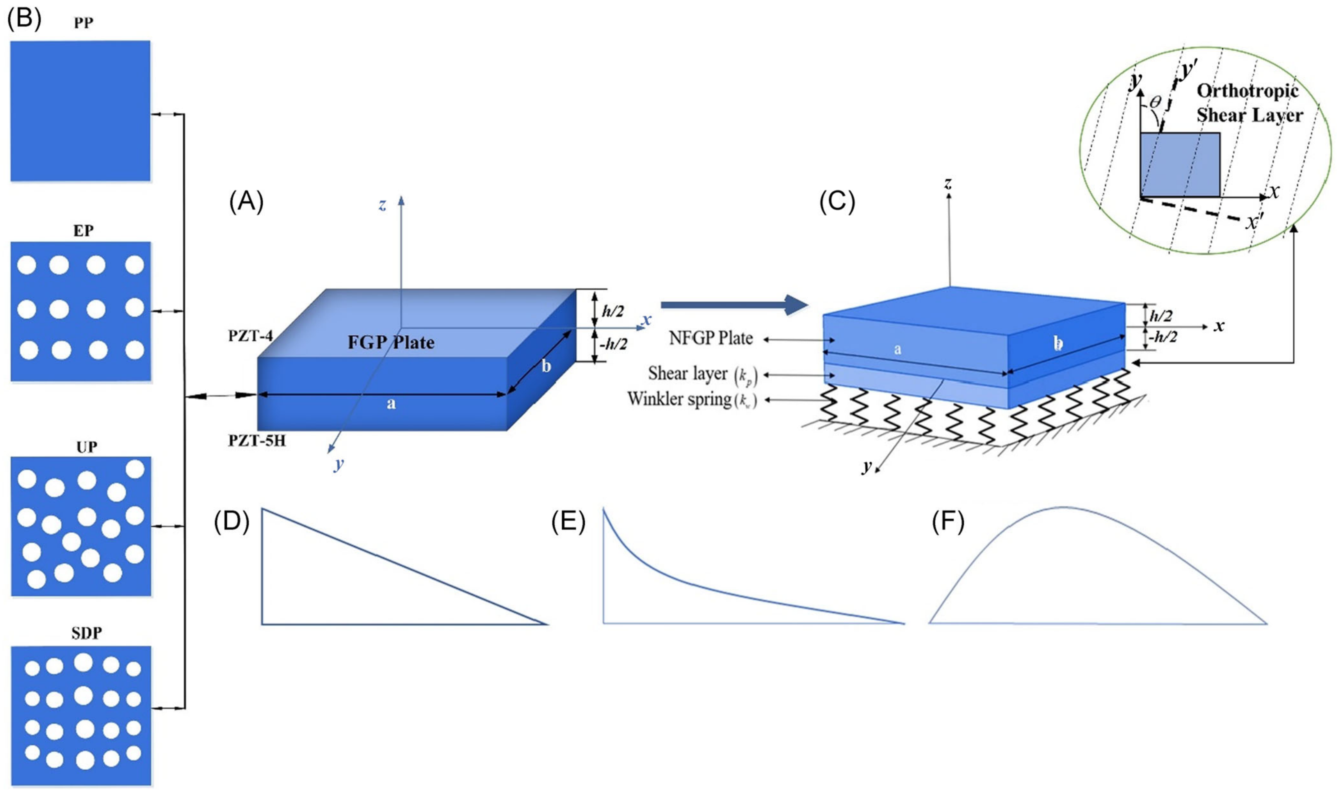

FIGURE 3 | FGP plate configurations (A) porosity distributions, (B) plate with foundations, and (C) different variations of foundations, that is, (D) linear, (E) parabolic, and (F) sinusoidal variations.

The general representation of the Pasternak foundations is as follows [40, 43, 76]:

$$q_{ef} = k_w w_0 - k_p \nabla^2 w_0. \tag{19}$$

The effect of orthotropic angles is explored in the current study by considering orthotropy in the foundation with respect to the global x-axis. This global axis provides the orthotropic angle θ, which is a Pasternak parameter for the foundation in the x- and y-directions. Therefore, the OPF can be represented as follows [40, 41, 43]:

$$q_{\mathrm{OPF}} = k_w w_0 - k_{px} A_1 - k_{py} A_2, \tag{20}$$

where $A_1 = \sin^2\theta w_{0,yy} + \cos^2\theta w_{0,xx} + \sin 2\theta w_{0,xy}$; $A_2 = \sin^2\theta\, w_{0,xx} + \cos^2\theta w_{0,yy} - \sin 2\theta w_{0,xy}$. k_w is the Winkler parameter and k_{px} and k_{py} are Pasternak parameters, respectively, and ∇^2 denotes the two-dimensional Laplace operator. In the present study, k_{px} and k_{py} are assumed to be constant, whereas k_w exhibits linear, quadratic, or sinusoidal variation along the axial direction (i.e., y-direction), as shown in Figure 3D–F. Specifically, they are defined as

$$\left.\begin{aligned} k_w &= \frac{12K_w a^4}{(C_{11})_{PT4}(h(y))^3}(1+\varsigma),\\ \varsigma &= \left\{\begin{array}{ll} \psi(x/a) & \text{for Linear (LF)}\\ \psi(x/a)^2 & \text{for Parabolic (PF)}\\ \psi\ \sin\ \pi(x/a) & \text{for Sinusoidal (SF)}\end{array}\right\},\\ k_{px} &= \frac{12K_{px}a^4}{(C_{11})_{PT4}(h(y))^3},\\ k_{py} &= \frac{12K_{py}a^4}{(C_{11})_{PT4}(h(y))^3}.\end{aligned}\right\} \tag{21}$$

where K_w, K_{px}, and K_{py}, are the Winkler's and Pasternak parameters. ψ is the varied parameter in the x-directions.

4 | Solution Technique

The multidirectional PFGN plate is discretized by nine-nodded isoparametric quadrilateral elements (Q9), with each node possessing six degrees of freedom (DOFs). These DOFs include three translational displacements $\{u_t\}$ or $\{u_0, v_0, w_0\}$, two bending rotations $\{u_r\}$ or $\{\varphi_1, \varphi_2\}$, and one electric potential Θ_0. These generalized coordinate vectors associated with the i^{th} node ($i = 1, 2, 3, \ldots, 9$) within each element can be expressed as [77]:

$$\left.\begin{aligned} \{\boldsymbol{u}_i\} &= \{u_{0i}\ v_{0i}\ w_{0i}\ \varphi_{1i}\ \varphi_{2i}\ \Theta_{0i}\},\\ \{\boldsymbol{u}_{ti}\} &= [u_{0i}\ v_{0i}\ w_{0i}]^{\mathrm{T}},\\ \{\boldsymbol{u}_{r_i}\} &= [\varphi_1\ \varphi_2]^{\mathrm{T}}.\end{aligned}\right\}, \tag{22}$$

The displacement field in the multidirectional PFGN plate element is interpolated using Lagrange shape functions and nodal displacements as follows:

$$\left.\begin{aligned} \{\boldsymbol{u}_t\} &= [\boldsymbol{N}_{ti}]\{\boldsymbol{u}_{ti}^e\};\ \{\boldsymbol{u}_r\} = [\boldsymbol{N}_{ri}]\{\boldsymbol{u}_{ri}^e\};\\ \{\boldsymbol{\Theta}_{0i}\} &= [\boldsymbol{N}_{\Theta i}]\{\boldsymbol{\Theta}_{0i}^e\};\ [\boldsymbol{u}_{0i}] = [\boldsymbol{N}_{ui}]\{\boldsymbol{u}_{ui}^e\};\\ [\boldsymbol{v}_{0i}] &= [\boldsymbol{N}_{vi}]\{\boldsymbol{u}_{vi}^e\};\ [\boldsymbol{w}_{0i}] = [\boldsymbol{N}_{wi}]\{\boldsymbol{u}_{wi}^e\};\\ [\varphi_{1i}] &= [\boldsymbol{N}_{\varphi_{1i}}]\{\boldsymbol{u}_{ri}^e\};\ [\varphi_{2i}] = [\boldsymbol{N}_{\varphi_{2i}}]\{\boldsymbol{u}_{ri}^e\};\end{aligned}\right\}, \tag{23}$$

where

$$\left.\begin{aligned}
&\left\{\boldsymbol{u}_{ti}^{e}\right\}=\left[\left\{\boldsymbol{u}_{t1}^{e}\right\}^{\mathrm{T}}\left\{\boldsymbol{u}_{t2}^{e}\right\}^{\mathrm{T}}\cdots\left\{\boldsymbol{u}_{t9}^{e}\right\}^{\mathrm{T}}\right]^{\mathrm{T}};\\
&\left\{\boldsymbol{u}_{ri}^{e}\right\}=\left[\left\{\boldsymbol{u}_{r1}^{e}\right\}^{\mathrm{T}}\left\{\boldsymbol{u}_{r2}^{e}\right\}^{\mathrm{T}}\cdots\left\{\boldsymbol{u}_{r9}^{e}\right\}^{\mathrm{T}}\right]^{\mathrm{T}};\left\{\boldsymbol{\Theta}_{0i}^{e}\right\}=\left[\Theta_{01}^{e}\ \Theta_{02}^{e}\cdots\Theta_{09}^{e}\right];\\
&[\boldsymbol{N}_{\Theta i}]=[N_1\ N_2\cdots N_9];\\
&[\boldsymbol{N}_{ti}]=[N_{t1}\ N_{t2}\cdots N_{t9}];\\
&[\boldsymbol{N}_{ri}]=[N_{r1}\ N_{r2}\cdots N_{r9}].
\end{aligned}\right\}\quad(24)$$

.

Here, N_i denotes the Lagrange shape function corresponding to the natural coordinates of the i^{th} node.

To derive the governing equations, Hamilton's principle is employed as follows [22, 37]

$$\delta\mathfrak{R}=\int_0^t\delta(\mathfrak{R}_{se}+\mathfrak{R}_{ef}+\mathfrak{R}_{wd}-\mathfrak{R}_{ke})\mathrm{d}t=0,\qquad(25)$$

where $\mathfrak{R}_{se}$, $\mathfrak{R}_{pe}$, $\mathfrak{R}_{wd}$, and $\mathfrak{R}_{ke}$ denote the strain energy, stored energy in the deformed elastic foundations, external work done, and kinetic energy, respectively. The strain energy is defined as follows:

$$\begin{aligned}
\delta\mathfrak{R}_{se}&=\int_V(\sigma_{11}\delta\varepsilon_{11}+\sigma_{22}\delta\varepsilon_{22}+k_{sf}\sigma_{23}\delta\gamma_{23}+k_{sf}\sigma_{13}\delta\gamma_{13}+\sigma_{12}\delta\gamma_{12}-D_1\delta E_1-D_2\delta E_2-D_3\delta E_3)\mathrm{d}V\\
&=\int_0^a\int_0^a\begin{pmatrix}(N_{11}\delta u_{0,x}+N_{22}\delta v_{0,y}+N_{12}(\delta u_{0,y}+\delta v_{0,x}))+(M_{11}\delta\varphi_{1,x}+M_{22}\delta\varphi_{2,y}+M_{12}(\delta\varphi_{1,y}+\delta\varphi_{2,x}))\\+\dfrac{N_{11}}{2}\delta(w_{0,x})^2+\dfrac{N_{22}}{2}\delta(w_{0,y})^2+N_{12}(\delta w_{0,x}\ \delta w_{0,y})+Q_{13}(\delta\varphi_1+\delta w_{0,x})+Q_{23}(\delta\varphi_2+\delta w_{0,y})\end{pmatrix}\mathrm{d}x\mathrm{d}y\qquad,\qquad(26)\\
&+\int_0^a\int_0^a\int_{-h(y)/2}^{h(y)/2}\left[-D_1\cos(\pi z/h(y))\delta\left(\frac{\partial\Theta_0}{\partial x}\right)-D_2\cos(\pi z/h(y))\delta\left(\frac{\partial\Theta_0}{\partial y}\right)-D_3(\pi/h(y))\sin(\pi z/h(y))\delta\Theta_0\right]\mathrm{d}z\mathrm{d}x\mathrm{d}y,
\end{aligned}$$

where k_{sf} is the shear correction factor, and the value is considered as 5/6. A shear correction factor (SCF) is introduced to overcome the shear locking phenomenon and to accurately capture the shear stress distribution, ensuring proper consideration of the nonuniform transverse shear strain in the plate. Additionally, the use of higher-order shape functions in the higher-order finite element (FE) method allows for more accurate displacement and strain interpolation, preventing the stiffness overestimation that typically arises due to shear-locking. Additionally, the stress resultants M, N, and Q in the multidirectional PFGN plate can be obtained by integrating the stress components in Equation (6) over the thickness. These stress resultants are defined as follows:

$$\left.\begin{aligned}
\{\boldsymbol{N}_{ij}\}&=\int_{-h(y)/2}^{h(y)/2}\{\sigma_{ij}\}\mathrm{d}z=\boldsymbol{A}\varepsilon_{bplr}+\boldsymbol{B}\varepsilon_{bpnlr}+N_{ij}^{EL}-N_{ij}^{TL}-N_{ij}^{HL};\ (i,j=1,2)\\
\{\boldsymbol{M}_{ij}\}&=\int_{-h(y)/2}^{h(y)/2}\{\sigma_{ij}\}z\mathrm{d}z;=\boldsymbol{B}\varepsilon_{bplr}+\boldsymbol{F}\varepsilon_{bpnlr}+M_{ij}^{EL}-M_{ij}^{TL}-M_{ij}^{HL};\ (i,j=1,2)\\
\{\boldsymbol{Q}_{i3}\}&=k_{sf}\int_{-h(y)/2}^{h(y)/2}\{\sigma_{i3}\}\mathrm{d}z=\boldsymbol{A}^{s}\varepsilon_{sp}+\boldsymbol{Q}_{i3}^{EL};\ \ i=1,2
\end{aligned}\right\}.\qquad(27)$$

Similarly, the hygrothermoelectrically-induced stress resultants are defined as follows:

$$\left.\begin{aligned}
&\left\{N_{ij}^{EL},M_{ij}^{EL}\right\}=\int_{-h(y)/2}^{h(y)/2}\bar{e}_{3ij}\left(\tfrac{2V}{h}\right)\{1,z\}\mathrm{d}z;\ i=1,2;j=1,2;\\
&\left\{N_{ij}^{TL},M_{ij}^{TL}\right\}=\int_{-h(y)/2}^{h(y)/2}\overline{C}_{1i}\bar{\alpha}(z)(T(z)-T_0)\{1,z\}\mathrm{d}z;\ i=1,2;j=1,2;\\
&\left\{N_{ij}^{HL},M_{ij}^{HL}\right\}=\int_{-h(y)/2}^{h(y)/2}\overline{C}_{1i}\bar{\beta}(z)(M(z)-M_0)\{1,z\}\mathrm{d}z;\ i=1,2;j=1,2;\\
&Q_{13}^{EL}=\int_{-h(y)/2}^{h(y)/2}\bar{e}_{15}\left(\tfrac{2z}{h(y)}\right)\mathrm{d}z\tfrac{\partial V}{\partial x}+\int_{-h(y)/2}^{h(y)/2}\bar{e}_{15}\left(\cos\tfrac{\pi z}{h(y)}\right)\mathrm{d}z\tfrac{\partial\Theta_0}{\partial x};\\
&Q_{23}^{EL}=\int_{-h(y)/2}^{h(y)/2}\bar{e}_{24}\left(\tfrac{2z}{h(y)}\right)\mathrm{d}z\tfrac{\partial V}{\partial x}+\int_{-h(y)/2}^{h(y)/2}\bar{e}_{24}\left(\cos\tfrac{\pi z}{h(y)}\right)\mathrm{d}z\tfrac{\partial\Theta_0}{\partial x}.
\end{aligned}\right\},\qquad(28)$$

where

$$\begin{aligned}
(\boldsymbol{A},\boldsymbol{B},\boldsymbol{F})&=\int_{-h(y)/2}^{h(y)/2}(C_{bp})\{1,z,z^2\}\mathrm{d}z;\\
(\boldsymbol{A}^{s})\qquad&=k_{sf}\int_{-h(y)/2}^{h(y)/2}(C_{sp})\mathrm{d}z;
\end{aligned}\qquad(29)$$

and $T(z)$ and $M(z)$ are the temperature and moisture variation within the plate, derived from Equations (16–18) under different conditions. The parameters T_0 and M_0 is the reference temperature and reference moisture, respectively. ΔT and ΔM are the changes in temperature and moisture concentrations on the top and bottom sides, respectively.

The kinetic energy $\delta\mathfrak{R}_{ke}$ is defined as:

$$\begin{aligned}
\delta\mathfrak{R}_{ke}&=\int_V\rho\left(\dot{u}_1^2+\dot{u}_2^2+\dot{u}_3^2\right)\mathrm{d}V\\
&=\int_S\left\{I_0\left(\dot{u}_0^2+\dot{v}_0^2+\dot{w}_0^2\right)+2I_1\left(\dot{u}_0\dot{\varphi}_1+\dot{v}_0\dot{\varphi}_2\right)\right.\\
&\quad\left.+I_2\left(\dot{\varphi}_1^2+\dot{\varphi}_2^2\right)\right\}\mathrm{d}x\mathrm{d}y,
\end{aligned}\qquad(30)$$

where the inertia terms I_0, I_1, and I_2 are defined as

$$(I_0,I_1,I_2)=\int_{-h(y)/2}^{h(y)/2}(1,z,z^2)\rho\mathrm{d}z.\qquad(31)$$

The strain energy of the variable elastic orthotropic foundations is expressed as

$$\delta\mathfrak{R}_{ef} = \int_S [(k_w w_0 - k_{px} A_1 - k_{py} A_2)\delta w_0 \mathrm{d}x\mathrm{d}y]. \tag{32}$$

The applied external work done is computed as follows:

$$\delta\mathfrak{R}_{wd} = \int_S [-q\delta w_0]\mathrm{d}x\mathrm{d}y, \tag{33}$$

where q is the transverse loading. N_{11}^{ML}, N_{22}^{ML} and N_{12}^{ML} are the mechanical force, while N_{11}^{EL} and N_{22}^{EL} are the electrical forces, N_{11}^{TL}, N_{11}^{HL} and N_{22}^{TL}, N_{22}^{HL} are the applied hygrothermal forces. The definitions of these forces are as follows:

$$\left.\begin{aligned} N_{11}^{ML} = N_{22}^{ML} = N^{ML}; \\ N_{12}^{ML} = 0; \\ N_{11}^{EL} = N_{22}^{EL} = N^{EL}; \\ N_{11}^{TL} = N_{22}^{TL} = N^{TL}; \\ N_{11}^{HL} = N_{22}^{HL} = N^{HL}. \end{aligned}\right\}, \tag{34}$$

The equations of motion for the multidirectional PFGN plate are obtained by substituting Equations (26–34) into Equation (24). These can be written as

$$\left.\begin{aligned} &\frac{\partial N_{11}}{\partial x} + \frac{\partial N_{12}}{\partial y} = \left(I_0 \ddot{u}_0^2 + I_1 \ddot{\varphi}_1^2\right); \frac{\partial N_{12}}{\partial x} + \frac{\partial N_{22}}{\partial y} = \left(I_0 \ddot{v}_0^2 + I_1 \ddot{\varphi}_2^2\right) \\ &\frac{\partial Q_{13}}{\partial x} + \frac{\partial Q_{23}}{\partial y} + (N^{ML} + N^{EL} - N^{TL} - N^{HL})\nabla^2 w_0 + (q - q_{OPF}) = I_0 \ddot{w}_0^2 \\ &\frac{\partial M_{11}}{\partial x} + \frac{\partial M_{12}}{\partial y} - Q_{13} = \left(I_1 \ddot{u}_0^2 + I_1 \ddot{\varphi}_1^2\right); \frac{\partial M_{12}}{\partial x} + \frac{\partial M_{22}}{\partial y} - Q_{23} = \left(I_1 \ddot{v}_0^2 + I_1 \ddot{\varphi}_2^2\right) \\ &\int_{-h(y)/2}^{h(y)/2} \left[D_{1,x} \cos\left(\frac{\pi z}{h(y)}\right) + D_{2,x} \cos\left(\frac{\pi z}{h(y)}\right) + \frac{\pi}{h(y)} \sin\left(\frac{\pi z}{h(y)}\right) D_3\right] \mathrm{d}z = 0 \end{aligned}\right\}. \tag{35}$$

The variational forms can be formulated by multiplying Equations (35) with the corresponding displacements, rotational and electric potential variables, integrating over the element domain, and adding the equation on each side. This leads to

$$\int_S \left[\begin{aligned} &(N_{11}\delta u_{0,x} + N_{22}\delta v_{0,y} + N_{12}(\delta u_{0,y} + \delta v_{0,x})) - (M_{11}\delta\varphi_{1,x} + M_{22}\delta\varphi_{2,y} + M_{12}(\delta\varphi_{1,y} + \delta\varphi_{2,x})) \\ &+ Q_{13}(\delta\varphi_1 + \delta w_{0,x}) + Q_{23}(\delta\varphi_2 + \delta w_{0,y}) - ((N^{ML} + N^{EL} - N^{TL} - N^{HL})\nabla^2 w_0 + (q - q_{OPF}))\delta w_0 \\ &-I_2(\dot{\varphi}_1\delta\dot{\varphi}_1 + \dot{\varphi}_2\delta\dot{\varphi}_2) - (I_0\dot{u}_0\delta\dot{u}_0 + \mathrm{I}_0\dot{v}_0\delta\dot{v}_0 + I_0\dot{w}_0\delta\dot{w}_0 + 2I_1(\dot{\varphi}_1\delta\dot{u}_0 + \dot{\varphi}_2\delta\dot{v}_0 + \dot{u}_0\delta\dot{\varphi}_1 + \dot{v}_0\delta\dot{\varphi}_2)) \\ &+\delta\Theta_0 \int_{-h(y)/2}^{h(y)/2} [D_{1,x} \cos(\pi z/h(y)) + D_{2,y} \cos(\pi z/h(y)) + D_3(\pi/h(y))\sin(\pi z/h(y))]\mathrm{d}z \end{aligned}\right] \mathrm{d}x\mathrm{d}y = 0. \tag{36}$$

The higher-order FE equation is derived by substituting Equations (22–24) into the weak-form Equation (36) and then rearranging and reassembling the equations based on the vector of nodal degree of freedom $\{\boldsymbol{u}\}$ in terms of displacements, rotations, and electric potentials. The generalized governing equation for the free vibration of the multidirectional PFGN porous plate is then given by:

$$[\boldsymbol{M}_g]\{\ddot{\boldsymbol{u}}\} + [\boldsymbol{K}_{eqv}]\{\boldsymbol{u}\} = \{\boldsymbol{F}\}, \tag{37}$$

where $[\boldsymbol{M}_g]$ the global mass matrix, $[\boldsymbol{K}_{eqv}]$ is the global stiffness matrix, (including the linear, nonlinear and geometric stiffness matrices), and $\{\boldsymbol{F}\}$ is the combined load vector, which includes the hygrothermal and electromechanical load vectors.

For the eigenvalue problem, Equation (38) is obtained by neglecting the effect of the hygrothermal force terms and including the effect of hygrothermal in the form of geometry matrices in Equation (37). The eigenvalue problem is stated as follows:

$$([\boldsymbol{K}_{eqv}] - \Omega^2[\boldsymbol{M}])\{\boldsymbol{u}\} = 0, \tag{38}$$

where Ω is the natural vibration frequency. The solutions to Equation (38) are obtained using the modified Newton-Raphson technique [77–79]. Note that the equivalent stiffness $[\boldsymbol{K}_{eqv}]$ is calculated as follows:

$$[\boldsymbol{K}_{eqv}] = [\boldsymbol{K}_{tt}] + [\boldsymbol{K}_{tr}] + [\boldsymbol{K}_{rr}] + [\boldsymbol{K}_{t\Theta}] + [\boldsymbol{K}_{r\Theta}] + [\boldsymbol{K}_{\Theta\Theta}]. \tag{39}$$

In Equation (39), $[\boldsymbol{K}_{tt}]$, $[\boldsymbol{K}_{tr}]$ and $[\boldsymbol{K}_{rr}]$ are the elastic stiffness matrices. $[\boldsymbol{K}_{t\Theta}]$ and $[\boldsymbol{K}_{r\Theta}]$ are piezoelectric-elastic coupling matrices, and $[\boldsymbol{K}_{\Theta\Theta}]$ is the elemental electric stiffness matrix.

5 | Results and Discussion

In this study, the free-vibration response analysis of the multidirectional PFGN plate under hygrothermal and thermoelectric conditions is analyzed. The material properties of the PFGM plate used in the study are listed in Table 1. The influence of various factors on the vibration responses of the nonuniform plates is thoroughly examined. These factors include the effects of thermal, electrical and moisture change, support conditions, thickness ratios, bidirectional material exponents, that is, n_z and n_x, thickness ratio (a/h), and porosity distribution with a porous exponent.

TABLE 1 | Material properties of the PFGN plates [16, 37].

Properties	$C_{11} = C_{22}$ **(GPa)**	C_{12} **(GPa)**	$C_{13} = C_{23}$ **(GPa)**	C_{33} **(GPa)**	$C_{44} = C_{55}$ **(GPa)**	C_{66} **(GPa)**	$e_{31} = e_{32}$ **(C/m^2)**
PZT-4	138.499	77.371	73.643	114.745	25.60	30.60	−5.2
PZT-5H	99.201	54.016	50.778	86.856	21.10	22.60	−7.209
Properties	$e_{15} = e_{24}$ (C/m^2)	e_{33} (C/m^2)	$\kappa_{11} = \kappa_{22}$ (C/Nm^2)	κ_{33} (C/Nm^2)	ρ(kg/m^3)	α(1/K)	β(m^3/kg)
PZT-4	12.72	15.08	1.306	1.115	7600	2×10^{-6}	1×10^{-4}
PZT-5H	12.322	15.118	1.530	1.500	7750	10×10^{-6}	1×10^{-4}

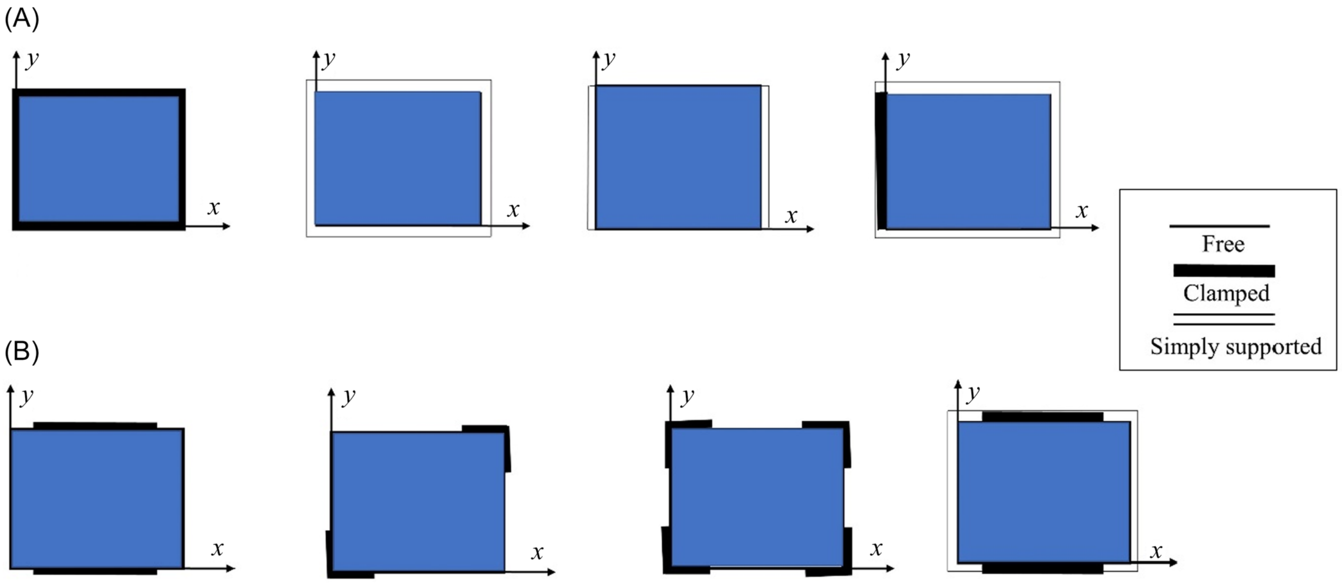

FIGURE 4 | Configurations of different boundary conditions (A) Conventional support conditions (CSC) (B) Unconventional support conditions (USC).

The PFGN plates are constrained by two types of support conditions (shown in Figure 4), namely conventional support conditions (CSC) and unconventional support conditions (USC). The considered CSC types are CCCC, SSSS, SFSF,and CFFF. The USC conditions are Case-1, Case-2, Case-3, and Case-4 types. The length of the USC boundary conditions along the plate's edge is defined by the clamped ratio (CR).

The clamping ratio (CR) is a critical parameter in defining the unconventional support conditions, as it quantifies the proportion of an edge that is clamped relative to the total length of the edge. The CR varies between 0 (no clamping) and 1 (fully clamped edge). In this analysis, a clamping ratio of 0.33 is considered for Case-1, with the clamping located in the middle of the two opposite y-constant edges. In Case-2, the clamping ratio is again 0.33, but the clamping is positioned at the two opposite corners, leaving the rest of the edges free. For Case-3, the clamping constraints are symmetrically located at the four corners, and the clamped ratio is 0.66. In Case-4, the CR is the same as in Case-1, but the remaining edges are simply supported instead of free, as in preceding cases.

The assumed geometrical parameter of the PFGN plate is adopted as $a/h = 20$ and $\beta_{tr} = 0.2$. The reference temperature and moisture are set to 300 K and 0% relative humidity, respectively. Additionally, boundary conditions on the electrical variables are associated with the electric potential, which may either be constant $\Theta = \Theta_0$ or vary with the position and time $\Theta = \Theta_0(x, y, t)$. The support conditions for each type are given below.

Boundary conditions parallel to x-axis:	*Boundary conditions parallel to y-axis*:
F: All degrees of freedom are nonzero.	**F**: All degrees of freedom are nonzero.
S: $u_0 = w_0 = \varphi_1 = \Theta = 0$; $v_0 = \varphi_2 \neq 0$	**S**: $v_0 = w_0 = \varphi_2 = \Theta = 0$; $u_0 = \varphi_1 \neq 0$
C: $u_0 = v_0 = w_0 = 0$; $\varphi_1 = \varphi_2 = \Theta = 0$	**C**: $u_0 = v_0 = w_0 = 0$; $\varphi_1 = \varphi_2 = \Theta = 0$

On the electrical side, boundary conditions are typically related to the electric potential or the electric displacement at the boundaries. One common electrical condition is applying a specific electric potential at the boundary, which can either be a constant $\Theta = \Theta_0$ or vary spatially with $\Theta = \Theta_0(x, y, t)$.

For simplicity, this analysis assumes the frequency parameter to be nondimensionalized as: $\omega = \Omega(a^2/h)\sqrt{(\rho/C_{11})_{PT4}}$, where Ω is the natural frequency, $(\rho)_{PT4}$ is the mass density, and $(C_{11})_{PT4}$ represents the elastic constants of the PZT-4 material.

TABLE 2 | Convergence behavior of the multidirectional PFGN plate's nondimensional frequency.

		Mesh element				
Plate configurations	**Thickness ratio (a/h)**	**12 × 12**	**14 × 14**	**16 × 16**	**18 × 18**	**20 × 20**
Plate A	20	1.6314	1.6307	1.6297	1.6291	1.6292
	50	2.0359	2.0351	2.0344	2.0339	2.0339
Plate B	20	2.1635	2.1628	2.1620	2.1617	2.1618
	50	2.5680	2.5671	2.5665	2.5659	2.5658

TABLE 3 | Comparison of the nondimensional frequency of the clamped FGM plate.

	Material exponent			
	$n_z = 2$		$n_z = 5$	
a/h	**Uymaz & Aydogdu [13]**	**Present**	**Uymaz & Aydogdu [13]**	**Present**
10	2.7658	2.7671	2.6645	2.6656
20	2.9765	2.9769	2.8844	2.8851
50	3.0479	3.0484	2.9597	2.9602

TABLE 4 | Assessment of the FGM plate's nondimensional frequency subjected to thermal loading.

	Material exponent					
	$n_z = 0.5$		$n_z = 1$		$n_z = 2$	
ΔT	**Huang & Shen [14]**	**Present**	**Huang & Shen [14]**	**Present**	**Huang & Shen [14]**	**Present**
0 K	7.1390	7.1402	6.6570	6.6576	6.2860	6.2866
100 K	7.1540	7.1549	6.5920	6.5927	6.2380	6.2385
300 K	6.7760	6.7766	6.3620	6.3624	6.0560	6.0567

TABLE 5 | Assessment of the tapered plate's nondimensional frequency.

	Tapered ratio			
	$\beta_{tr} = 0.25$		$\beta_{tr} = 0.50$	
a/h	**Manna [15]**	**Present**	**Manna [15]**	**Present**
5	19.057	19.062	20.518	20.525
10	21.224	21.228	23.282	23.288
100	22.164	22.171	24.543	24.549

TABLE 6 | Comparison of the nondimensional natural frequency of the FGM plate.

	$Wmax/h$			
Method	**0.2**	**0.4**	**0.6**	**0.8**
Present	1.028	1.088	1.187	1.303
Huang and Shen [14]	1.021	1.082	1.176	1.296
Behjat and Khoshravan [16]	1.027	1.089	1.189	1.309

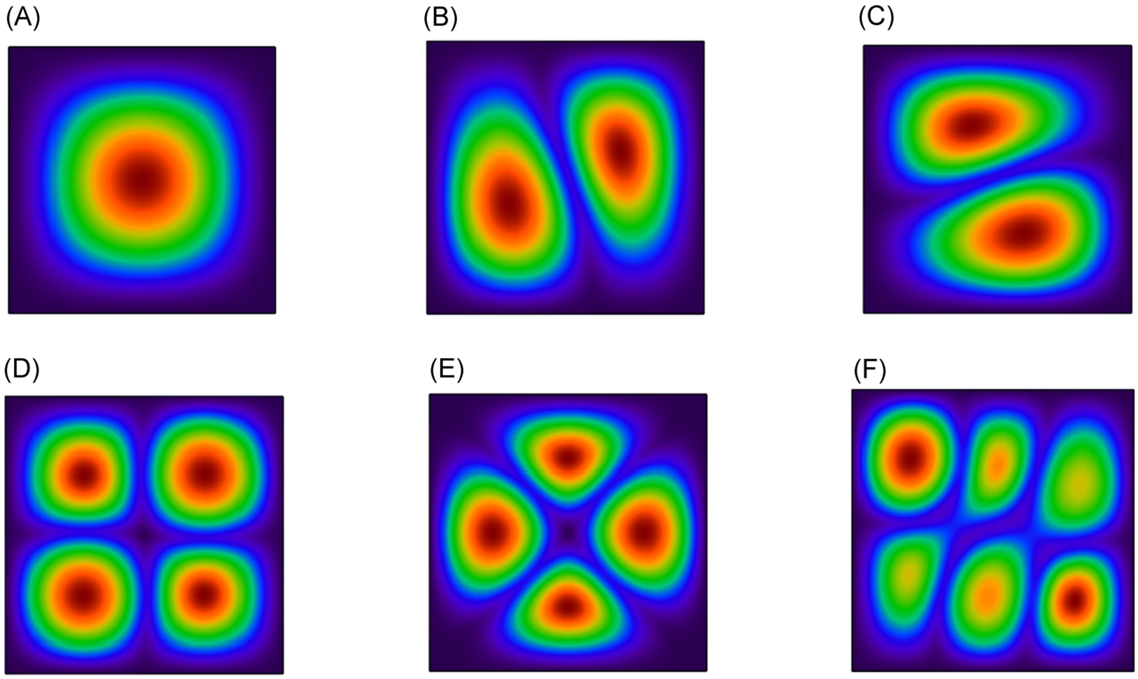

FIGURE 5 | First six mode shapes of Plate A (uniform thickness) with nondimensional frequency: (A) First (2.0566), (B) Second (6.4666), (C) Third (6.4666), (D) Fourth (9.9966), (E) Fifth (12.1966), (F) Sixth (12.3972).

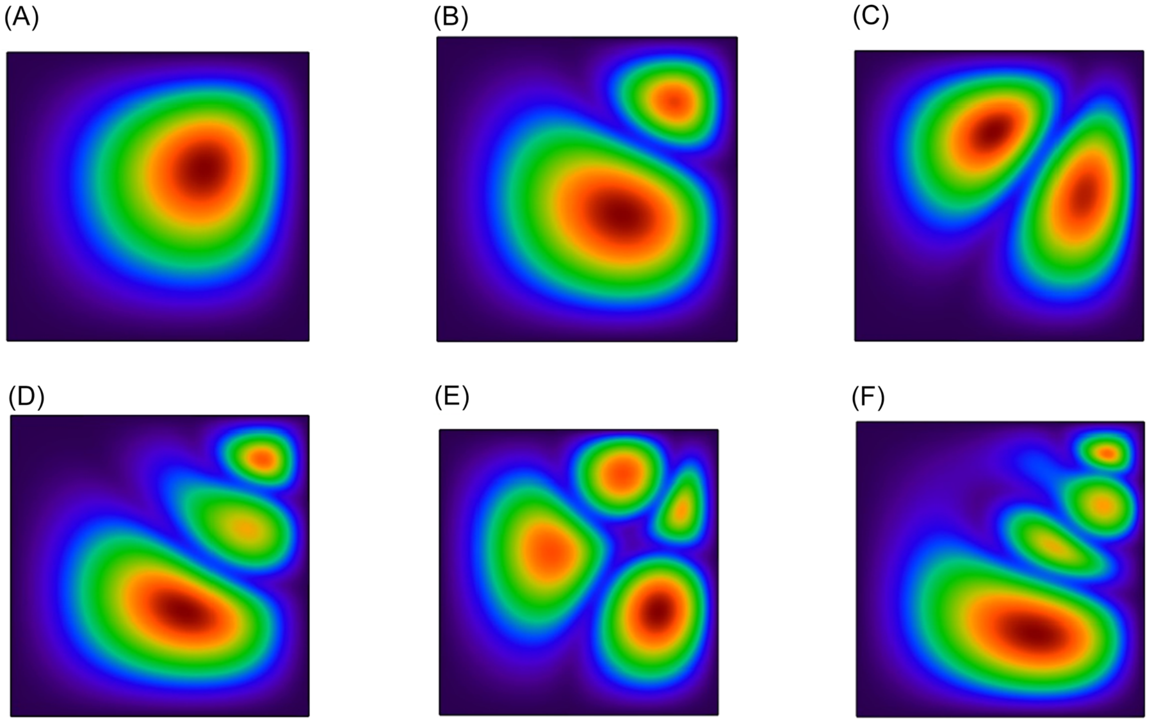

FIGURE 6 | First six mode shapes of Plate B (nonuniform thickness) with nondimensional frequency: (A) First (2.3887), (B) Second (6.7987), (C) Third (6.7987), (D) Fourth (10.3287), (E) Fifth (12.5287), (F) Sixth (12.7317).

5.1 | Convergence

The convergence of the current model is assessed by estimating the free vibration results. For the convergence analysis, the free vibration responses of the bidirectional clamped multidirectional PFGN plate are calculated and presented in Table 2. The assumed plate parameters $n_z = n_x = 5$ are considered without porosity and foundations. Table 2 indicates that optimum convergence is achieved with an 18 mesh ×18 mesh refinement, which is also appropriate for determining the PFGN plate's nonlinear frequency.

5.2 | Validations

The accuracy and effectiveness of the present formulations of the multidirectional PFGN plate are investigated using some existing problems.

Example 1: The problem investigates the nondimensional frequency of the clamped Al/ZrO2-based plate. The assumed plate dimensions are $a/h = 10$, 20, and 50 with different material exponents. The properties of the FG plate are the same as those in Uymaz and Aydogdu [13]. Table 3 displays a good agreement between the current and the literature results.

Example 2: This example compares the effect of the temperature change on the nondimensional frequency of the SSSS FGM plate. The FGM plate consists of Ti-6Al-4V and ZrO_2 materials. The material and geometrical properties are identical to those in Huang and Shen [14]. The results presented in Table 4 show good agreement with Huang and Shen's [14] result.

Example 3: This problem examines the frequency responses of the isotropic rectangular tapered clamped plate. The assumed plate dimensions are $a/h = 5$, 10, and 100, with tapered ratios of 0.25 and 0.50. The material properties of the rectangular tapered plate are similar to those in Manna [15]. The results, shown in Table 5, demonstrate good agreement with the Manna's [15] findings.

Example 4: This problem presents the first nondimensional natural frequency of a clamped FGM plate and compares the results with those obtained by Huang and Shen [14] and Behjat and Khoshravan [16] for different values of the material exponent. To ensure consistency, all material and geometrical properties used in this analysis are taken from Behjat and Khoshravan [16]. The results, as shown in Table 6, demonstrate

TABLE 7 | Assessment of the nondimensional frequency of the Perfect PFGN plate A with CSC and USC at $a/h = 20$, $\beta_{tr} = 0$, and $\theta = 0°$.

(n_z)	(n_x)	CCCC	SSSS	SFSF	CFFF	CASE-1	CASE-2	CASE-3	CASE-4
1	1	2.2546	1.2865	0.9484	0.5348	1.1014	0.5741	1.3104	2.2345
	2	2.0701	1.2206	0.8825	0.4689	1.0355	0.5082	1.2445	2.1686
	5	1.8856	1.1547	0.8166	0.4030	0.9696	0.4423	1.1786	2.1027
2	1	2.1201	1.2385	0.9004	0.4868	1.0534	0.5261	1.2624	2.1865
	2	2.0566	1.1974	0.8874	0.4108	0.9124	0.4405	1.2104	2.0145
	5	1.8721	1.1315	0.8215	0.3449	0.8465	0.3746	1.1445	1.9486
5	1	2.0356	1.2083	0.8702	0.4566	1.0232	0.4959	1.2322	2.1563
	2	1.9722	1.1747	0.8647	0.3881	0.8897	0.4178	1.1877	1.9918
	5	1.9691	1.1099	0.7999	0.3233	0.8249	0.3530	1.1229	1.9270
10	1	1.9511	1.1761	0.8380	0.4244	0.9910	0.4637	1.2000	2.1241
	2	1.9237	1.1574	0.8474	0.3708	0.8724	0.4005	1.1704	1.9745
	5	1.9156	1.0909	0.7809	0.3043	0.8059	0.3340	1.1039	1.9080

TABLE 8 | Assessment of the nondimensional frequency of the perfect PFGN plate B with CSC and USC at $a/h = 20$, $\beta_{tr} = 0.1$, and $\theta = 0°$.

(n_z)	(n_x)	CCCC	SSSS	SFSF	CFFF	CASE-1	CASE-2	CASE-3	CASE-4
1	1	2.7124	1.7985	1.5280	1.0547	1.5847	1.0426	1.7451	2.6987
	2	2.5269	1.7323	1.4618	0.9885	1.5185	0.9764	1.6789	2.6325
	5	2.3414	1.6660	1.3955	0.9222	1.4522	0.9101	1.6126	2.5662
2	1	2.5769	1.7501	1.4796	1.0063	1.5363	0.9942	1.6967	2.6503
	2	2.5887	1.7295	1.4195	0.9429	1.4445	0.9124	1.6823	2.4864
	5	2.4032	1.6633	1.3533	0.8767	1.3783	0.8462	1.6161	2.4202
5	1	2.3914	1.6839	1.4134	0.9401	1.4701	0.9280	1.6305	2.5841
	2	2.3270	1.7065	1.3965	0.9199	1.4215	0.8894	1.6593	2.4634
	5	2.5012	1.6421	1.3321	0.8555	1.3571	0.8249	1.5948	2.3989
10	1	2.3059	1.6517	1.3812	0.9079	1.4379	0.8958	1.5983	2.5519
	2	2.2784	1.6892	1.3792	0.9026	1.4042	0.8720	1.6419	2.4460
	5	2.4468	1.6226	1.3126	0.8360	1.3376	0.8055	1.5754	2.3795

TABLE 9 | Variation of the CCCC constraint Plate A frequency with variable elastic foundations and porosity distributions at $a/h = 20$, $\beta_{tr} = 0$, $kp = 20$, and $\theta = 0°$.

		LF		PF		SF	
Porosity distribution	**(*kw*,*Ψ*)**	$n_z = n_x = 2$	$n_z = n_x = 5$	$n_z = n_x = 2$	$n_z = n_x = 5$	$n_z = n_x = 2$	$n_z = n_x = 5$
PP ($\Upsilon = 0$)	(20,10)	2.5545	2.1042	2.9670	2.5167	2.3444	2.5545
	(50,30)	2.9544	2.5041	3.3669	2.9166	2.7443	2.9544
	(80,50)	3.3543	2.9040	3.7668	3.3165	3.1442	3.3543
EP ($\Upsilon = 0.2$)	(20,10)	2.5978	2.1475	3.0103	2.5600	2.3876	2.5978
	(50,30)	3.3543	2.9040	3.7668	3.3165	3.1442	3.3543
	(80,50)	3.7542	3.3039	4.1667	3.7164	3.5441	3.7542
UP ($\Upsilon = 0.2$)	(20,10)	2.6412	2.1909	3.0537	2.6034	2.4311	2.6412
	(50,30)	3.7542	3.3039	4.1667	3.7164	3.5441	3.7542
	(80,50)	4.1541	3.7038	4.5666	4.1163	3.9440	4.1541
SCP ($\Upsilon = 0.2$)	(20,10)	2.6848	2.2345	3.0973	2.6470	2.4747	2.6848
	(50,30)	4.1554	3.7051	4.5679	4.1176	3.9453	4.1554
	(80,50)	4.5553	4.1050	4.9678	4.5175	4.3452	4.5553

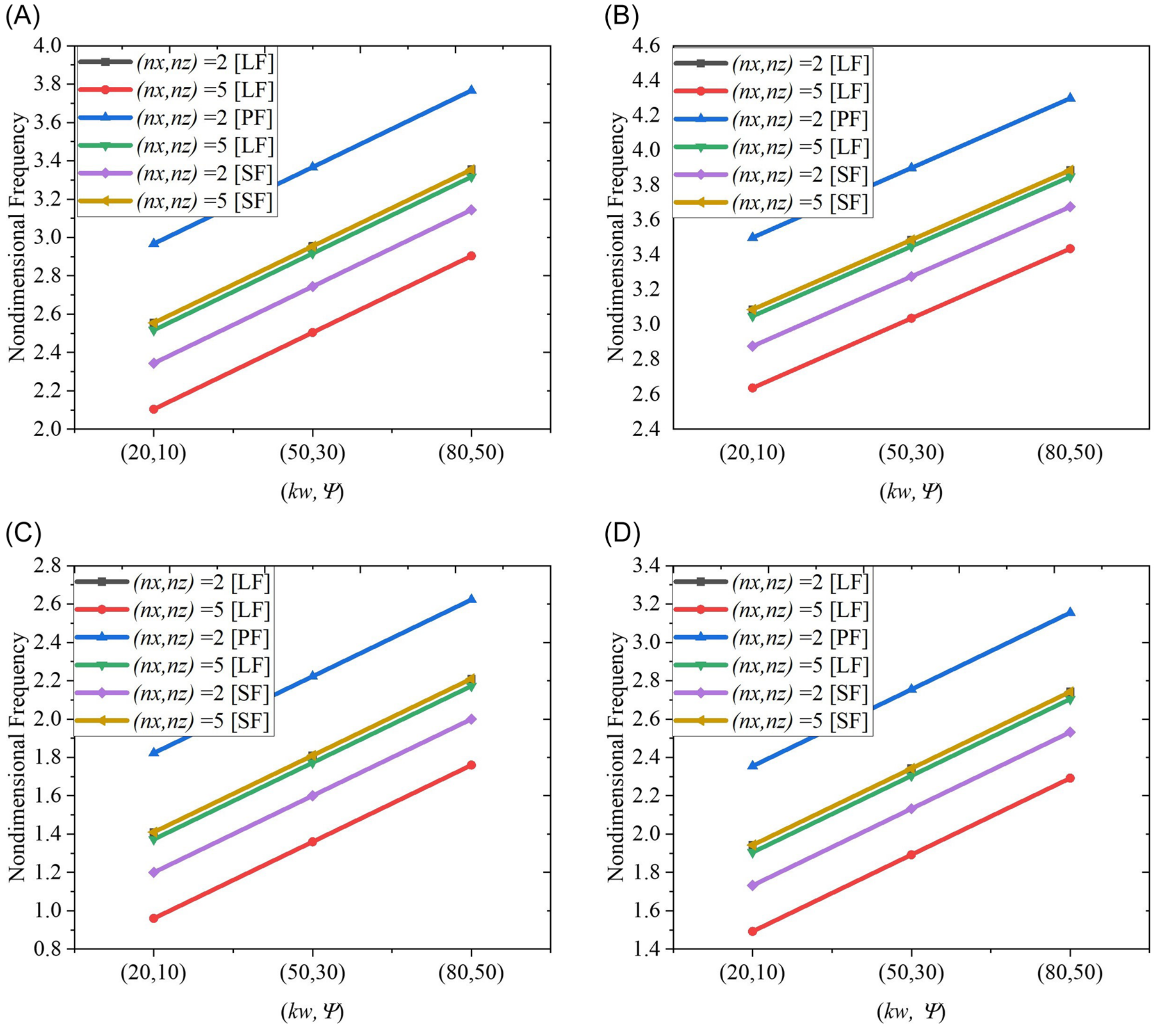

FIGURE 7 | Influence of the varied elastic foundation with n_x and n_z exponent on the frequency of the PFGN perfect plate at $kp = 20$, $\theta = 0°$, and $a/h = 20$: (A) CCCC, Plate A, (B) CCCC, Plate B, (C) Case 1, Plate A, and (D) CCCC, Plate B.

TABLE 10 | Variations of frequency of the CCCC Plate B with tapered ratios, thickness ratio, and the orthotropic angle at $k_w = 20$, $k_{px} = 20$, $k_{py} = 10$, $\Psi = 10$ (LF), and $n_z = n_x = 2$.

		PP		EP ($\Upsilon = 0.2$)		UP ($\Upsilon = 0.2$)		SCP ($\Upsilon = 0.2$)	
a/h	β_{tr}	$\theta = 30°$	$\theta = 45°$	$\theta = 30°$	$\theta = 45°$	$\theta = 30°$	$\theta = 45°$	$\theta = 30°$	$\theta = 45°$
10	0.1	2.6717	2.5593	2.7150	2.6025	2.7583	2.6458	2.8015	2.6891
	0.3	2.7132	2.6008	2.7565	2.6440	2.7998	2.6873	2.8430	2.7306
	0.5	2.7547	2.6423	2.7980	2.6855	2.8413	2.7288	2.8845	2.7721
20	0.1	2.9742	2.8617	3.0174	2.9050	3.0607	2.9482	3.1040	2.9915
	0.3	3.0157	2.9032	3.0589	2.9465	3.1022	2.9897	3.1455	3.0330
	0.5	3.0572	2.9447	3.1004	2.9880	3.1437	3.0312	3.1870	3.0745
30	0.1	3.2766	3.1641	3.3199	3.2074	3.3632	3.2507	3.4064	3.2940
	0.3	3.3181	3.2056	3.3614	3.2489	3.4047	3.2922	3.4479	3.3355
	0.5	3.3596	3.2471	3.4029	3.2904	3.4462	3.3337	3.4894	3.3770
40	0.1	3.5791	3.4666	3.6223	3.5099	3.6656	3.5531	3.7089	3.5964
	0.3	3.6206	3.5081	3.6638	3.5514	3.7071	3.5946	3.7504	3.6379
	0.5	3.6621	3.5496	3.7053	3.5929	3.7486	3.6361	3.7919	3.6794
50	0.1	3.8815	3.7690	3.9248	3.8123	3.9680	3.8556	4.0113	3.8988
	0.3	3.9230	3.8105	3.9663	3.8538	4.0095	3.8971	4.0528	3.9403
	0.5	3.9645	3.8520	4.0078	3.8953	4.0510	3.9386	4.0943	3.9818

TABLE 11 | Variations of frequency of Case 1 Plate B with different tapered ratios, thickness ratio, and the orthotropic angle at $k_w = 20$, $k_{px} = 20$, $k_{py} = 10$, $\Psi = 10$ (LF), and $n_z = n_x = 2$.

		PP		EP($\Upsilon = 0.2$)		UP($\Upsilon = 0.2$)		SCP($\Upsilon = 0.2$)	
a/h	β_{tr}	$\theta = 30°$	$\theta = 45°$	$\theta = 30°$	$\theta = 45°$	$\theta = 30°$	$\theta = 45°$	$\theta = 30°$	$\theta = 45°$
10	0.1	1.8240	1.7055	1.8683	1.7448	1.9126	1.7891	1.9568	1.8334
	0.3	1.8671	1.7486	1.9114	1.7879	1.9557	1.8322	1.9999	1.8765
	0.5	1.9102	1.7917	1.9545	1.8310	1.9988	1.8753	2.0430	1.9196
20	0.1	2.1465	2.0280	2.1907	2.0673	2.2350	2.1115	2.2793	2.1558
	0.3	2.1896	2.0711	2.2338	2.1104	2.2781	2.1546	2.3224	2.1989
	0.5	2.2327	2.1142	2.2769	2.1535	2.3212	2.1977	2.3655	2.2420
30	0.1	2.4689	2.3504	2.5132	2.3897	2.5574	2.4340	2.6017	2.4782
	0.3	2.5120	2.3935	2.5563	2.4328	2.6005	2.4771	2.6448	2.5213
	0.5	2.5551	2.4366	2.5994	2.4759	2.6436	2.5202	2.6879	2.5644
40	0.1	2.7913	2.6729	2.8356	2.7121	2.8799	2.7564	2.9241	2.8007
	0.3	2.8344	2.7160	2.8787	2.7552	2.9230	2.7995	2.9672	2.8438
	0.5	2.8775	2.7591	2.9218	2.7983	2.9661	2.8426	3.0103	2.8869
50	0.1	3.1138	2.9953	3.1580	3.0346	3.2023	3.0788	3.2466	3.1231
	0.3	3.1569	3.0384	3.2011	3.0777	3.2454	3.1219	3.2897	3.1662
	0.5	3.2000	3.0815	3.2442	3.1208	3.2885	3.1650	3.3328	3.2093

excellent agreement with the existing literature, validating the accuracy and reliability of the proposed approach.

5.3 | Parametric Study

This section presents the parametric analysis of the various influencing parameters on the free-vibration response of the multidirectional PFGN plate resting on a VOPF. The parameters analyzed include thickness ratio, porous exponent, multi-directional material exponents, different support conditions (CSC and USC), VOPF, and thermoelectric and hygrothermal loading.

Figures 5 and 6 illustrate the first six mode shapes of the multidirectional PFGN plate with uniform and variable

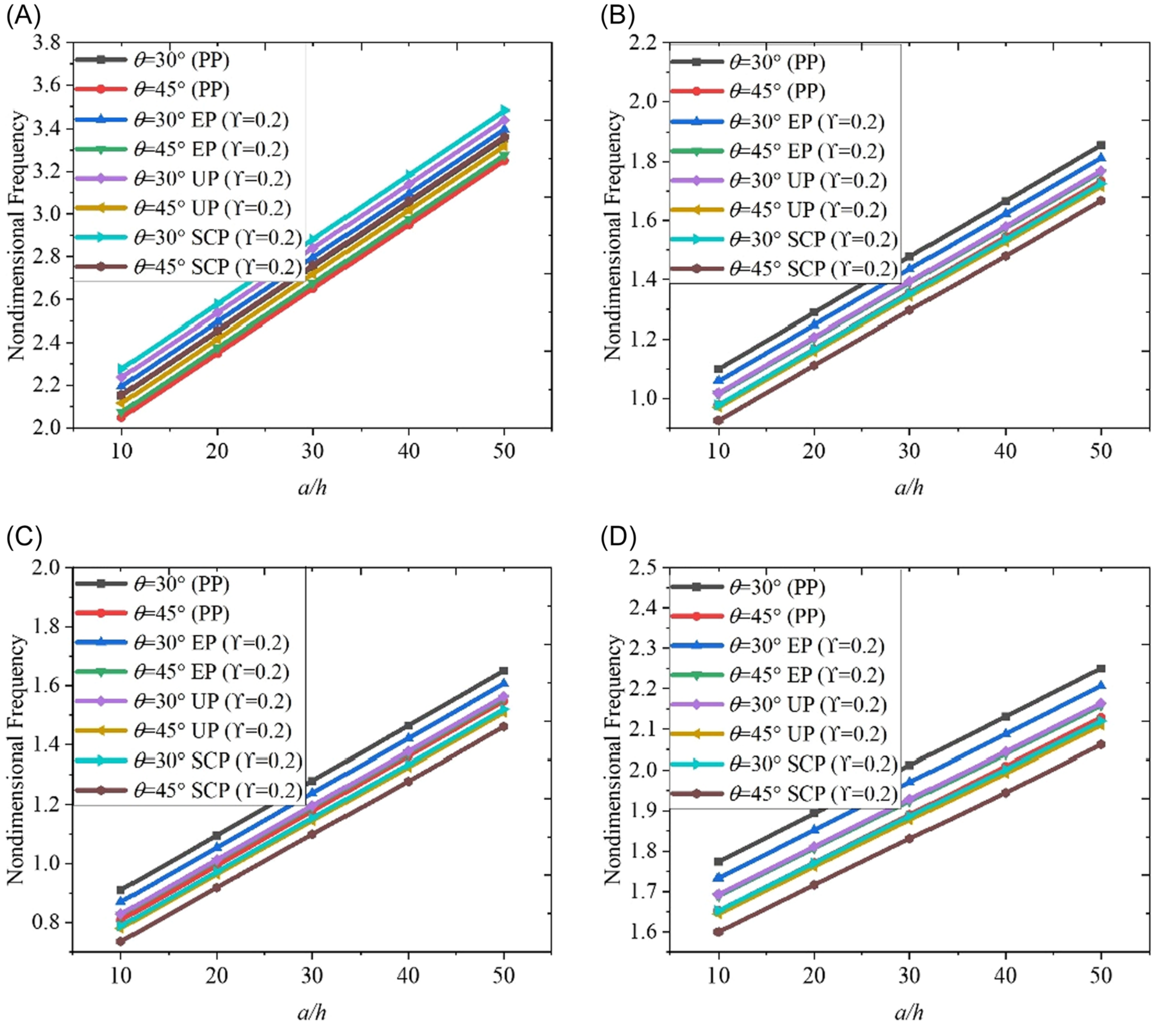

FIGURE 8 | Influence of the thickness ratio with porosity and exponent on the frequency of the PFGN plate at $k_w = 20$, $k_{px} = 20$, $k_{py} = 10$, $\Psi = 10$ (LF), and $n_z = n_x = 2$: (A) Plate A, CCCC, (B) Plate A, Case 1, (C) Plate A, SSSS, (D) Plate A, Case 4.

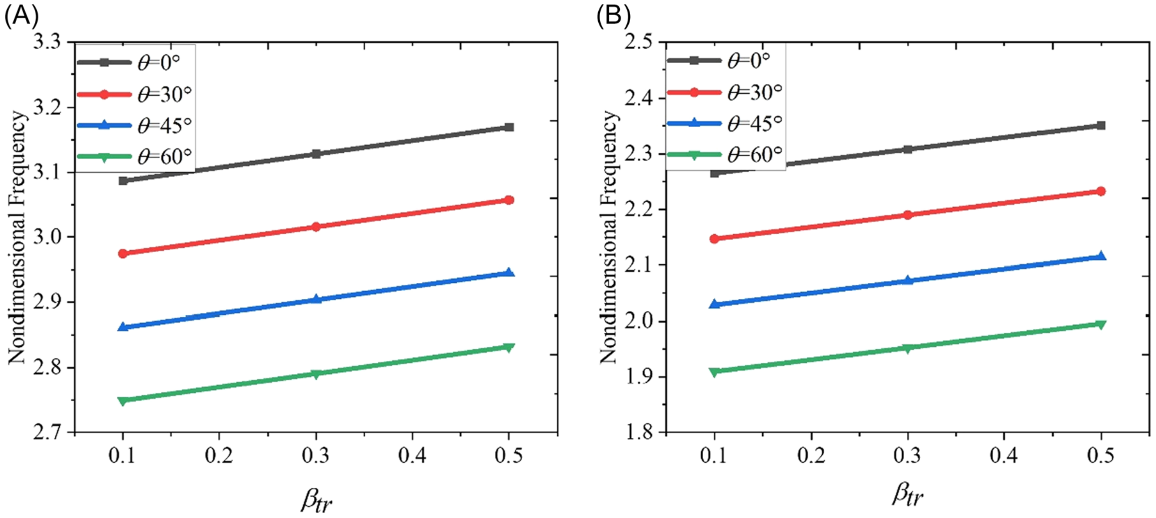

FIGURE 9 | Influence of the orthotropic angles in OPF with a tapered ratio on the frequency of the PFGN perfect plate at $k_w = 20$, $k_{px} = 20$, $k_{py} = 10$, $\Psi = 10$ (LF), and $(n_z, n_x) = 2$: (A) Plate B, CCCC, (B) Plate B, Case 1.

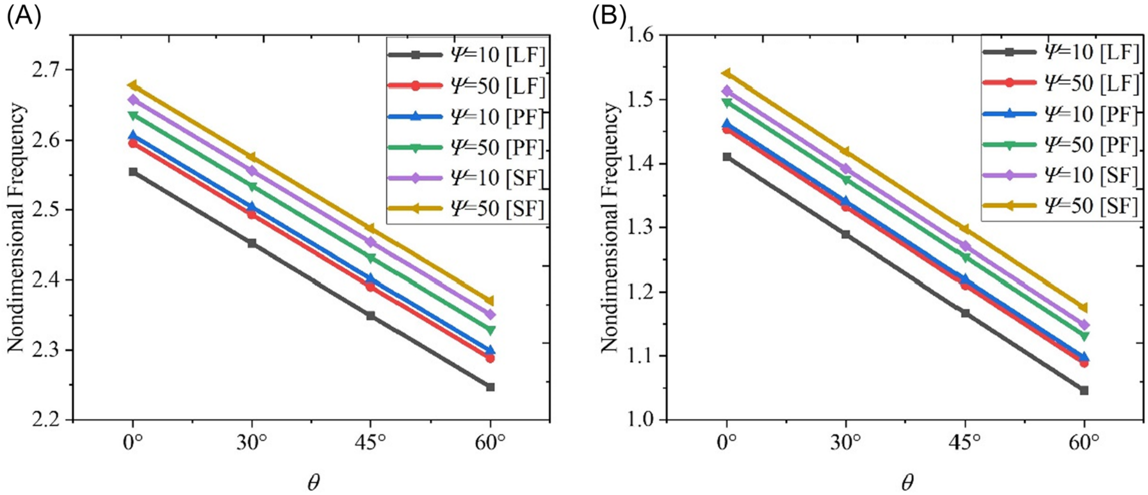

FIGURE 10 | Influence of the orthotropic angles and varied parameters in the VOPF with different elastic foundations on the frequency of the PFGN plate at $k_w = 20$, $k_{px} = 20$, $k_{py} = 10$, $n_z = n_x = 2$, and $a/h = 20$: (A) Plate A, CCCC, (B) Plate A, Case 1.

TABLE 12 | Effect of the hygrothermal loading and the orthotropic angle on the frequency response of CCCC Plate A at UHT, $a/h = 20$, $k_w = 20$, $k_{px} = 20$, $k_{py} = 10$, and $\Psi = 10$ (LF).

		$(\Delta T, \Delta M) = (0, 0)$				**$(\Delta T, \Delta M) = (20, 1)$**				**$(\Delta T, \Delta M) = (40, 2)$**			
		n_z				**n_z**				**n_z**			
θ	n_x	**1**	**2**	**5**	**10**	**1**	**2**	**5**	**10**	**1**	**2**	**5**	**10**
0°	1	2.254	2.105	2.014	2.003	2.123	1.931	1.801	1.767	1.992	1.757	1.587	1.531
	2	2.154	2.056	2.008	1.987	2.023	1.882	1.795	1.751	1.892	1.708	1.581	1.515
	5	2.015	1.998	1.969	1.943	1.884	1.824	1.755	1.707	1.753	1.650	1.541	1.471
30°	1	2.176	2.051	1.976	1.979	2.045	1.877	1.763	1.743	1.914	1.703	1.549	1.506
	2	2.075	2.002	1.970	1.962	1.944	1.828	1.757	1.726	1.813	1.654	1.543	1.490
	5	1.937	1.944	1.931	1.919	1.806	1.770	1.717	1.682	1.675	1.596	1.503	1.446
45°	1	2.075	1.976	1.922	1.945	1.944	1.802	1.709	1.708	1.813	1.628	1.495	1.472
	2	1.974	1.928	1.916	1.928	1.843	1.753	1.703	1.692	1.712	1.579	1.489	1.456
	5	1.835	1.869	1.877	1.884	1.704	1.695	1.663	1.648	1.573	1.521	1.449	1.412
60°	1	2.001	1.935	1.890	1.917	1.869	1.761	1.676	1.681	1.738	1.587	1.462	1.445
	2	1.899	1.886	1.884	1.901	1.768	1.712	1.670	1.665	1.637	1.538	1.457	1.429
	5	1.761	1.828	1.844	1.857	1.630	1.654	1.631	1.621	1.499	1.480	1.417	1.385

thickness types under CCCC conditions at $a/h = 20$, $\Upsilon = 0$, $n_z = n_x = 2$, $\theta = 0^o$(no foundations), $\beta_{tr} = 0.1$ (for plate B), and with $\Delta T = \Delta M = 0$. These mode shapes represent the actual behavior (deformations) of the multidirectional piezoelectric functionally graded uniform and nonuniform thickness plate at a particular frequency.

Tables 7 and 8 show the frequencies of the perfect PFGN plate A ($\beta_{tr} = 0$) and Plate B ($\beta_{tr} = 0.1$) under CSC and USC conditions, with different material exponents n_x and n_z. The assumed parameters are $a/h = 20$, $\theta = 0°$(no foundations), and $\Delta T = \Delta M = 0$. Note that the material exponents significantly impact its stiffness and dynamic response. A higher material exponent generally results in a more pronounced material variation, leading to lower natural frequencies. As the exponents increase from 1 to 10, the contents of the p4-type material decrease, which reduces the stiffness of the plates. Initially, the *x*-direction material exponent has a more dominant effect on the frequency than the *z*-direction material component, but as the *z*-direction exponent increases from 1 to 10, the effect of the *x*-direction material exponent diminishes due to the gradation properties.

Additionally, tapering affects the stiffness distribution. The thicker section of Plate B provides higher rigidity, while the thinner end introduces flexibility, leading to variations in vibration characteristics. Hence, the nondimensional frequency of the nonuniform plate B is always higher than the uniform plate A. Furthermore, boundary conditions play a crucial role. The natural frequencies for the CCCC case are higher in the CSC condition. Among the USC cases, Case 4 exhibits the highest natural frequency because the more rigid constraints applied to the other two edges of the plate.

Table 9 presents the impact of the frequency on the CCCC constrained Plate A with variable elastic foundations and different porosity distribution and material exponents. The assumed dimensional parameters of the plate are $a/h = 20$, $k_p = 20$, $\Upsilon = 0.2$ and $\theta = 0°$. The porous exponent is taken as 0.2, meaning the plate has a controlled level of porosity that affects its stiffness and mass distribution. Notably, no orthotropic foundation effects are considered, meaning the elastic foundation is isotropic rather than having direction-dependent stiffness.

The results show that the nondimensional frequency increases with rising k_w and ψ. In the SF cases, the frequency values decrease due to their periodic flexibility, while in the PF cases, the frequency increases by enhancing stiffness in critical areas compared to the LF cases. Additionally, the multidirectional PFGN plate exhibits higher nondimensional frequency in the SCP distribution compared to the EP and UP distributions. This is because in the SCP distribution, microvoids or pores are symmetrically located near the center of the plate, maintaining a more balanced stiffness profile. In contrast, in EP and UP distributions, the porosity is either concentrated at the edges or uniformly spread, which leads to a greater reduction in overall stiffness, thereby lowering the frequency response.

Figure 7 depicts the impact of variable elastic foundations and different values of the material exponents n_x and n_z on the

TABLE 13 | Effect of the hygrothermal loading and the orthotropic angle on the frequency response of CCCC Plate A at LHT, PP, $a/h = 20$, $k_w = 20$, $k_{px} = 20$, $k_{py} = 10$, and $\Psi = 10$ (LF).

		(ΔT, ΔM) = (0, 0)				**(ΔT, ΔM) = (20, 1)**				**(ΔT, ΔM) = (40, 2)**			
		n_z				n_z				n_z			
θ	n_x	1	2	5	10	1	2	5	10	1	2	5	10
0°	1	2.403	2.301	2.241	2.269	2.272	2.127	2.027	2.033	2.141	1.953	1.813	1.797
	2	2.302	2.252	2.235	2.253	2.171	2.078	2.021	2.017	2.040	1.904	1.807	1.781
	5	2.163	2.194	2.195	2.209	2.032	2.020	1.981	1.973	1.901	1.846	1.768	1.737
30°	1	2.324	2.247	2.203	2.244	2.193	2.073	1.989	2.008	2.062	1.899	1.775	1.772
	2	2.224	2.198	2.197	2.228	2.093	2.024	1.983	1.992	1.962	1.850	1.770	1.756
	5	2.085	2.140	2.157	2.184	1.954	1.966	1.944	1.948	1.823	1.792	1.730	1.712
45°	1	2.223	2.172	2.149	2.210	2.092	1.998	1.935	1.974	1.961	1.824	1.721	1.738
	2	2.122	2.123	2.143	2.194	1.991	1.949	1.929	1.958	1.860	1.775	1.715	1.722
	5	1.984	2.065	2.103	2.150	1.853	1.891	1.890	1.914	1.722	1.717	1.676	1.678
60°	1	2.148	2.131	2.116	2.183	2.017	1.957	1.903	1.947	1.886	1.783	1.689	1.711
	2	2.048	2.082	2.110	2.167	1.917	1.908	1.897	1.930	1.786	1.734	1.683	1.694
	5	1.909	2.024	2.071	2.123	1.778	1.850	1.857	1.887	1.647	1.676	1.643	1.650

TABLE 14 | Effect of the hygrothermal loading and the orthotropic angle on the frequency response of CCCC Plate A at NHT, PP, $a/h = 20$, $k_w = 20$, $k_{px} = 20$, $k_{py} = 10$, and $\Psi = 10$ (LF).

		(ΔT, ΔM) = (0,0)				**(ΔT, ΔM) = (20,1)**				**(ΔT, ΔM) = (40,2)**			
		n_z				n_z				n_z			
θ	n_x	1	2	5	10	1	2	5	10	1	2	5	10
0°	1	2.444	2.353	2.303	2.324	2.313	2.179	2.089	2.088	2.182	2.005	1.875	1.852
	2	2.344	2.304	2.297	2.308	2.213	2.130	2.083	2.072	2.082	1.956	1.870	1.836
	5	2.205	2.246	2.257	2.264	2.074	2.072	2.044	2.028	1.943	1.898	1.830	1.792
30°	1	2.366	2.299	2.265	2.300	2.235	2.125	2.051	2.064	2.104	1.951	1.838	1.828
	2	2.265	2.250	2.259	2.283	2.134	2.076	2.046	2.047	2.003	1.902	1.832	1.811
	5	2.127	2.192	2.220	2.240	1.996	2.018	2.006	2.003	1.865	1.844	1.792	1.767
45°	1	2.264	2.224	2.211	2.266	2.133	2.050	1.997	2.030	2.002	1.876	1.784	1.793
	2	2.164	2.175	2.205	2.249	2.033	2.001	1.991	2.013	1.902	1.827	1.778	1.777
	5	2.025	2.117	2.166	2.205	1.894	1.943	1.952	1.969	1.763	1.769	1.738	1.733
60°	1	2.190	2.183	2.179	2.238	2.059	2.009	1.965	2.002	1.928	1.835	1.751	1.766
	2	2.089	2.134	2.173	2.222	1.958	1.960	1.959	1.986	1.827	1.786	1.745	1.750
	5	1.950	2.076	2.133	2.178	1.819	1.902	1.919	1.942	1.688	1.728	1.706	1.706

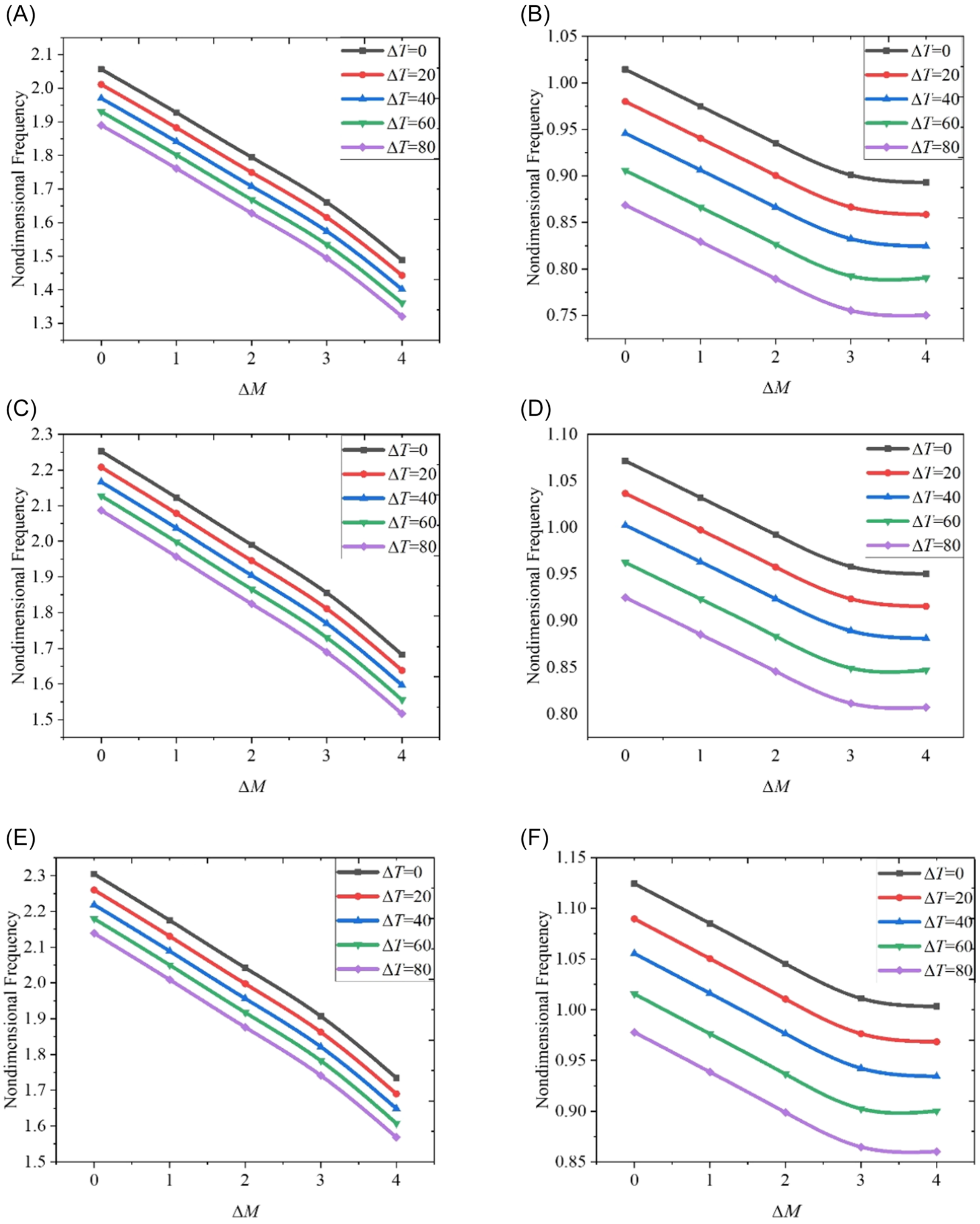

FIGURE 11 | Effect of the hygrothermal parameter on the PFGN perfect plate A frequency at $\theta = 0°$, $n_z = n_x = 2$ and $a/h = 20$: (A) CCCC, UHT, (B) Case 1, UHT, (C) CCCC, LHT, (D) Case 1, LHT, (E) CCCC, NHT, (F) Case 1, NHT.

frequency parameters of the multidirectional PFGN plate at constant $k_p = 20$ and $a/h = 20$, with the perfect plate configuration. The results indicate that an increase in the elastic foundation parameters enhances the structural rigidity, leading to higher nondimensional natural frequency. Additionally, the material exponents significantly affect the vibrational response. Lower exponent values increase the stiffness and yield higher frequencies.

Tables 10 and 11 present the effects of the orthotropic angle, tapered ratio, and thickness ratio of the multidirectional PFGN Plate B on the nondimensional frequency under the CCCC and Case-1 boundary conditions. The assumed geometrical properties are $k_w = 20$, $k_{px} = 20$, $k_{py} = 10$, $\psi = 10$ (LF), and $n_z = n_x = 2$. The comparison between the CCCC and Case-1 conditions shows that the plate frequency decreases with an increase in the orthotropic angle for different thickness ratios ($a/h = 10$, 20, 30, 40, 50) and tapered ratios ($\beta_{tr} = 0.1, 0.2, 0.3$). This trend is consistent across the other variable foundations (SF and PF) and boundary conditions (CSC and USC). Additionally, the multidirectional PFGN plate frequency decreases

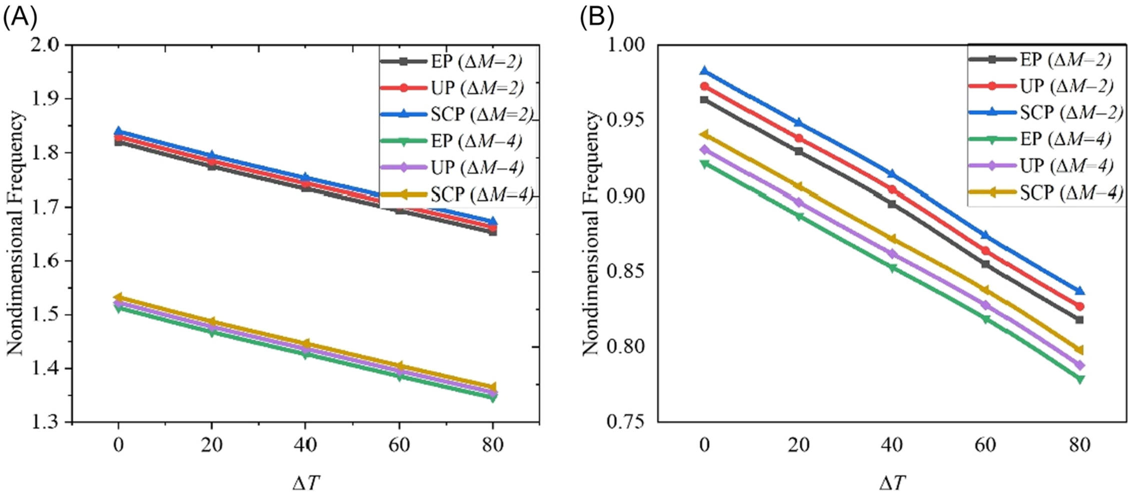

FIGURE 12 | Effect of the temperature and moisture change with porosity distribution on the PFGN Plate A type frequency at $\theta = 0°$, $\Upsilon = 0.2$, $n_z = n_x = 2$, and $a/h = 20$: (A) CCCC, UHT, (B) Case 1, UHT.

as the tapered ratio increases from 0.1 to 0.3. This reduction is due to the decrease in effective stiffness, causing instability in numerical solution, while a reduction in effective inertia at certain levels of porosity contributes to unstable solutions.

Figure 8 illustrates the frequency response of the multidirectional PFGN plate under the CCCC, SSSS, Case 1, and Case 4 conditions, influenced by the orthotropic angle and thickness ratios, with constant $k_w = 20$, $k_{px} = 20$, $k_{py} = 10$, $\psi = 10$ (LF), and $n_z = n_x = 2$. It is observed that the frequency of the plate decreases as the orthotropic angle increases with the thickness ratio. The frequency is directly proportional to the plate's stiffness, and since Young's modulus is inversely proportional to the mass of porous plates, thinner plates exhibit enhanced structural stiffness. Among the different porosity distributions, the perfect plate (PP) at $\theta = 30°$ shows the highest frequency, highlighting superior stiffness compared to porous structures. Plates with evenly distributed and symmetrically centered porosity configurations exhibit lower frequencies due to material reduction, with the SCP distribution showing the lowest stiffness. The CCCC boundary condition results in the highest frequency, while the SSSS condition yields slightly lower frequencies. Cases 1 and 4, which involve unconventional boundary conditions, show reduced frequency values compared to the fully clamped cases.

Figure 9 shows the influence of the tapered ratio and orthotropic angle on the frequency behavior of the plate, with $k_w = 20$, $k_{px} = 20$, $k_{py} = 10$, $\psi = 10$ (LF), and $n_z = n_x = 2$. The results indicate that the frequency increases with the tapered ratio, as the plate becomes thicker and stiffer, whereas the frequency decreases with an increase in the orthotropic angle.

Figure 10 shows the effect of varied parameters of different elastic foundations and orthotropic angles on the frequency behavior of the nonporous plate at constants $k_w = 20$, $k_{px} = 20$, $k_{py} = 10$, $n_z = n_x = 2$, and $a/h = 20$. It is found that the effect of the varied parameters on the plate's frequency is significant, with higher values of the varied parameters leading to a larger impact on the frequency. Additionally, the influence of the support conditions is notable. More constraints or restrictions on the edges of the plate result in an increase in the frequency. Thus, variable foundations are found to be more suitable for applications subjected to significant or variable excitations to avoid response variations.

Tables 12–14 illustrate the frequency response of the multidirectional PFGN CCCC Plate A, considering variations in temperature and moisture change, material exponent n_x, and n_z, and the orthotropic angle of the linearly varying foundations, under different hygrothermal loading types: uniform hygrothermal (UHT) (Table 12), linear hygrothermal (LHT) (Table 13), and nonlinear hygrothermal (UHT) (Table 14) loading. The assumed plate dimension is $a/h = 20$ along with the foundation parameters $k_w = 20$, $k_{px} = 20$, $k_{py} = 10$, and $\Psi = 10$ (LF). The results indicate that the frequency of the multidirectional PFGN plate decreases as the hygrothermal loading (i.e., temperature change ΔT and moisture change ΔM) increases from $(\Delta T, \Delta M) = (0,0)$ to $(40,2)$. This reduction is primarily due to the increase in moisture and temperatures, which lowers the overall rigidity of the structure. As the material softens under hygrothermal variations, the plate becomes more flexible, leading to greater deformations and lower natural frequencies.

Among the three types of hygrothermal loading considered (UHT, LHT, and NHT), the nonlinear hygrothermal loading (NHT) has the most significant impact on the frequency. NHT introduces more complex variations in temperature and moisture across the plate, resulting in a greater reduction in overall stiffness, particularly in regions with higher thermal or moisture concentration. The nonlinear nature of these variations exacerbates the material softening, thereby reducing the frequency more than in the linear or uniform cases.

Additionally, the material exponents in both the thickness and axial directions influence the frequency. Both exponents cause a reduction in frequency; however, material exponents in the axial direction have a greater effect on reducing the frequency compared to those in the thickness direction. This is because material variations in the axial direction more directly affect the plate's in-plane stiffness, which plays a larger role in its overall vibrational

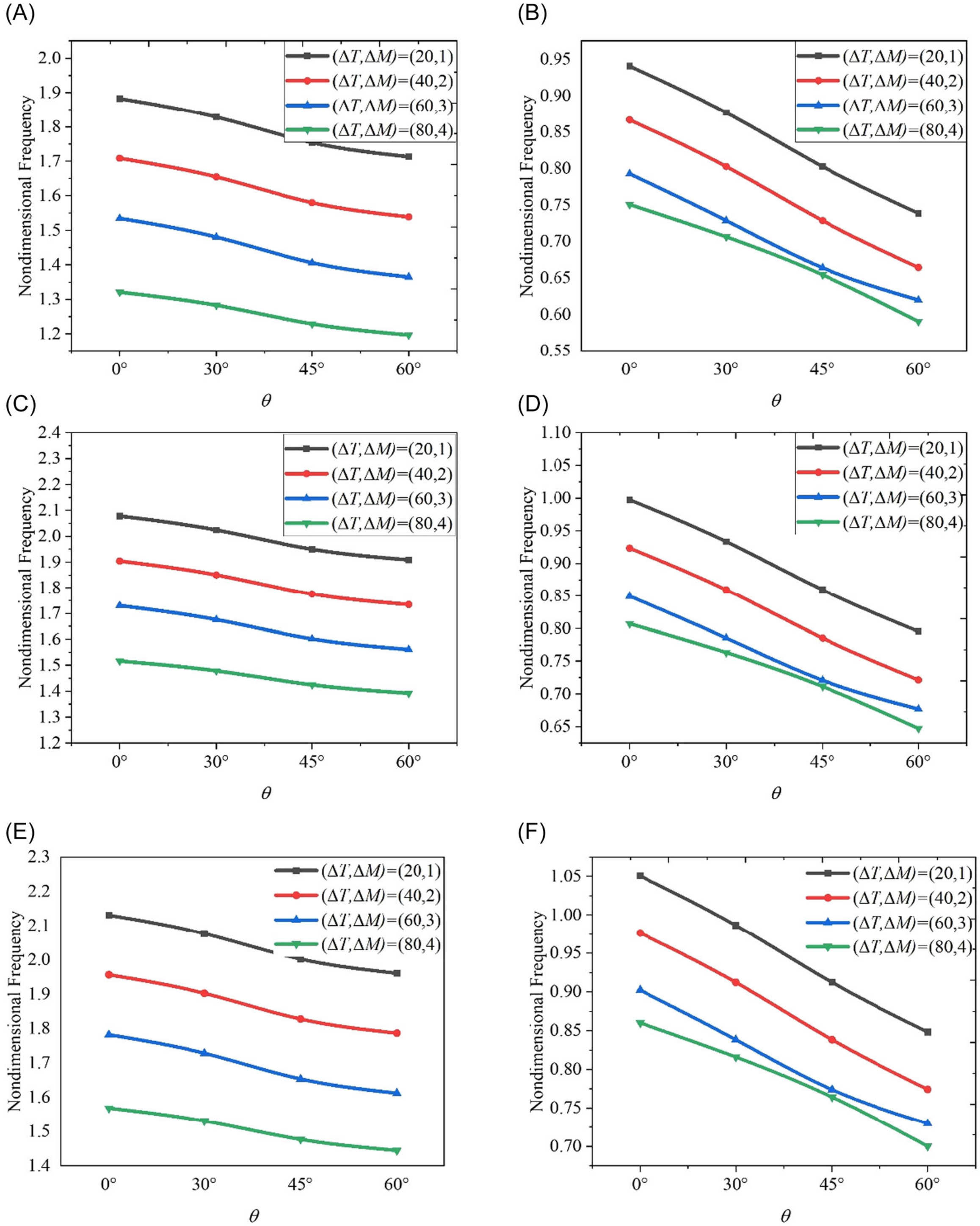

FIGURE 13 | Influence of the hygrothermal parameters with different orthotropic angles on the frequency of the PFGN perfect Plate A at $k_w = 20$, $k_{px} = 20$, $k_{py} = 10$, $n_z = n_x = 2$, and $a/h = 20$: (A) CCCC, UHT, (B) Case 1, UHT, (C) CCCC, LHT, (D) Case 1, LHT, (E) CCCC, NHT, (F) Case 1, NHT.

behavior. The effects of material exponents, hygrothermal loading, and the orthotropic angle of the variable elastic foundations on the PFGN plate subjected to both CSC and USC support conditions follow a similar trend, as observed in Tables 12–14.

Figure 11 presents the frequency response of Plate A under constant $\theta = 0°$, $n_z = n_x = 2$ and $a/h = 20$, subjected to different hygrothermal loading conditions (UHT, LHT, and NHT). The results show that the frequency decreases as temperature and moisture rise, primarily because both factors reduce the plate's stiffness, making the structure more flexible. Among the hygrothermal loading conditions, NHT introduces more complex variations in temperature and moisture distribution across the plate, causing a greater reduction in stiffness, particularly in areas where temperature and moisture are more concentrated.

Figure 12 shows the impact of the porosity distribution with variations in temperature and moisture change, on the frequency

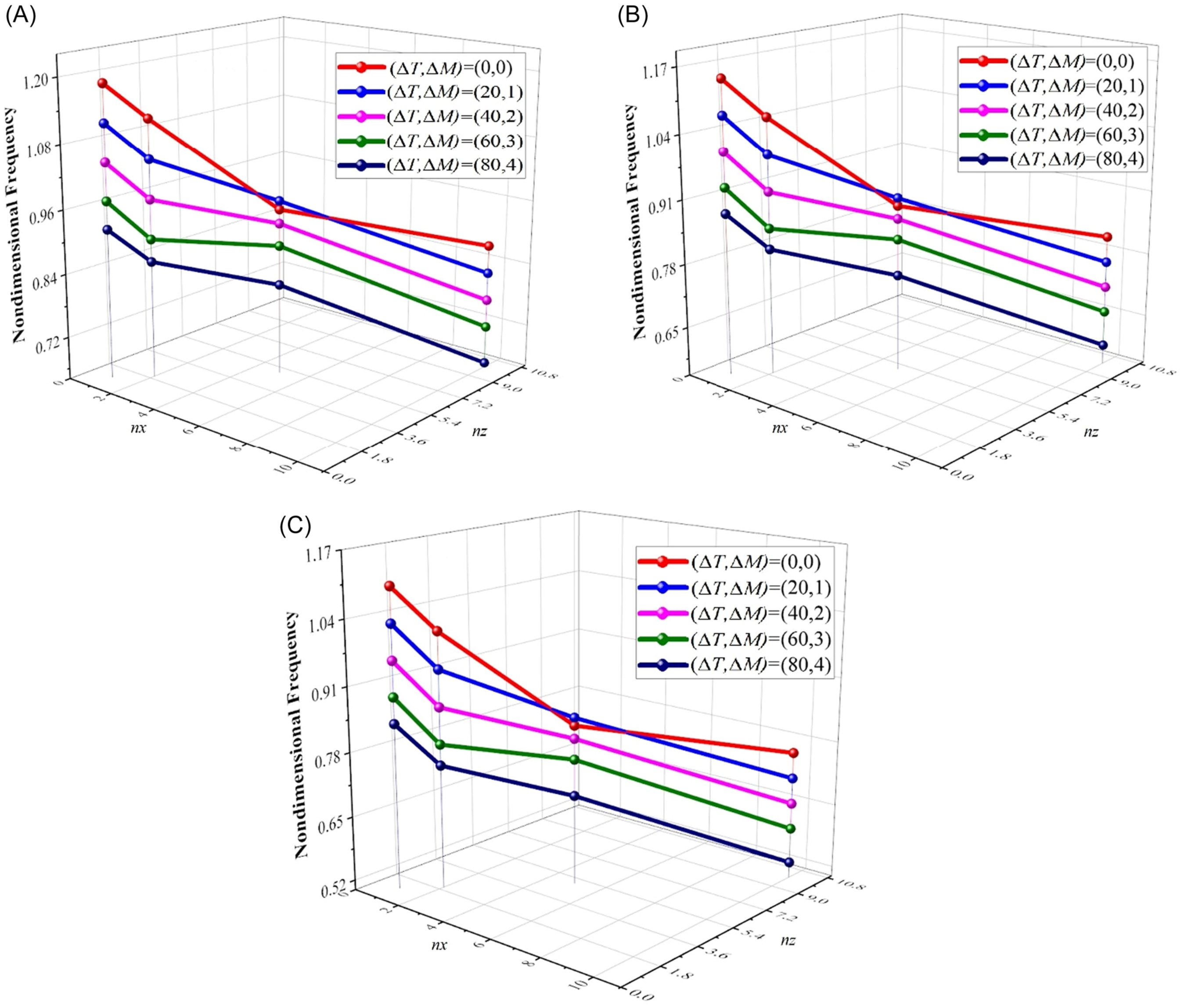

FIGURE 14 | Influence of the (n_z, n_x) and hygrothermal parameters on frequency of the perfect Case 1 PFGN Plate A at $a/h = 20$ and $\theta = 0°$: (A) Case 1, NHT, (B) Case 1, LHT, (C) Case 1, UHT.

response of the PFGN Plate under constant $\theta = 0°$, $\Upsilon = 0.2$, $n_z = n_x = 2$ and $a/h = 20$. It is observed that the SCP distribution has a more significant influence on the plate's frequency compared to the EP and UP distributions. The SCP distribution places microvoids or pores symmetrically at the center of the plate, leading to a more balanced reduction in stiffness across the structure. This symmetrical arrangement helps maintain a more stiffness profile, which results in higher natural frequencies compared to the other two distributions, where the porosity is either concentrated evenly or uniformly spread.

Figure 13 displays the impact of the orthotropic angle and hygrothermal change on the frequency of the PFGN Plate A at $n_z = n_x = 2$ and $a/h = 20$. The frequency response of the plate decreases as the orthotropic angle increases from 0° to 60° at constant foundation parameters $k_w = 20$, $k_{px} = 20$, and $k_{py} = 10$ under CCCC and Case 1 conditions. Different hygrothermal conditions, namely, LHT, UHT, and NHT are considered. The frequency responses are highly affected by variations in temperature and moisture change. This trend is expected to remain consistent in all other CSC and USC conditions.

Figure 14 demonstrates the impact of the material exponent with hygrothermal parameters on the frequency response Case 1 PFGN Plate A, with $a/h = 20$ and $\theta = 0°$. It is observed that increasing the hygrothermal parameters decreases the frequency. This is because the rise in hygrothermal parameters lowers the overall stiffness of the plates. Additionally, both the material exponent (n_z, n_x) significantly affect the frequency behavior, as the natural frequency is directly related to the plate stiffness.

Tables 15 and 16 show the effect of the electromechanical loading, thickness ratio, and tapered ratio on the frequency variations of the PFGN Plate B under CCCC and Case 1 conditions. The assumed geometrical parameters for Plate B are $k_w = 20$, $k_{px} = 20$, $k_{py} = 10$, $\Psi = 10$ (LF), and $n_z = n_x = 2$. It is observed that both the tapered ratio and the thickness ratio have an increasing effect on the frequency of the plate. As these ratios increase, the natural frequency also increases. However, the

TABLE 15 | Variations of the frequency of CCCC PFGN perfect plate B with thickness ratio, tapered ratio, and electrical loading at $k_w = 20$, $k_{px} = 20$, $k_{py} = 10$, $\Psi = 10$ (LF), and $n_z = n_x = 2$.

		$\theta = 0°$			$\theta = 30°$		
a/h	**β_{tr}**	**$V = 50$**	**$V = 0$**	**$V = -50$**	**$V = 50$**	**$V = 0$**	**$V = -50$**
10	0.1	2.7783	2.7842	2.7922	2.6658	2.6717	2.6797
	0.3	2.8198	2.8257	2.8337	2.6717	2.7132	2.7547
	0.5	2.8613	2.8672	2.8752	2.7132	2.7547	2.7962
20	0.1	3.0808	3.0866	3.0956	2.9683	2.9742	2.9832
	0.3	2.8613	3.1281	2.8752	2.7132	3.0157	2.7962
	0.5	2.9028	3.1696	2.9167	2.7547	3.0572	2.8377
30	0.1	3.3832	3.3891	3.3992	3.2707	3.2766	3.2867
	0.3	2.9028	3.4306	2.9167	2.7547	3.3181	2.8377
	0.5	2.9443	3.4721	2.9582	2.7962	3.3596	2.8792
40	0.1	3.6856	3.6915	3.7031	3.5732	3.5791	3.5906
	0.3	2.9443	3.7330	2.9582	2.7962	3.6206	2.8792
	0.5	2.9858	3.7745	2.9997	2.8377	3.6621	2.9207
50	0.1	3.9881	3.9940	4.0069	3.8756	3.8815	3.8944
	0.3	2.9858	4.0355	2.9997	2.8377	3.9230	2.9207
	0.5	3.0273	4.0770	3.0412	2.8792	3.9645	2.9622

TABLE 16 | Variations of the frequency of the Case 1 PFGN perfect plate B with thickness ratio, tapered ratio, and electrical loading at $k_w = 20$, $k_{px} = 20$, $k_{py} = 10$, $\Psi = 10$ (LF), and $n_z = n_x = 2$.

		$\theta = 0°$			$\theta = 30°$		
a/h	**β_{tr}**	**$V = 50$**	**$V = 0$**	**$V = -50$**	**$V = 50$**	**$V = 0$**	**$V = -50$**
10	0.1	1.9356	1.9425	1.9507	1.8171	1.8240	1.8322
	0.3	1.9771	1.9856	1.9922	1.8256	1.8671	1.9086
	0.5	2.0186	2.0287	2.0337	1.8687	1.9102	1.9517
20	0.1	2.2580	2.2649	2.2641	2.1396	2.1465	2.1457
	0.3	2.0186	2.3080	2.0337	1.8671	2.1896	1.9501
	0.5	2.0601	2.3511	2.0752	1.9102	2.2327	1.9932
30	0.1	2.5805	2.5874	2.5776	2.4620	2.4689	2.4591
	0.3	2.0601	2.6305	2.0752	1.9086	2.5120	1.9916
	0.5	2.1016	2.6736	2.1167	1.9517	2.5551	2.0347
40	0.1	2.9029	2.9098	2.8910	2.7844	2.7913	2.7725
	0.3	2.1016	2.9529	2.1167	1.9501	2.8344	2.0331
	0.5	2.1431	2.9960	2.1582	1.9932	2.8775	2.0762
50	0.1	3.2254	3.2322	3.2045	3.1069	3.1138	3.0860
	0.3	2.1431	3.2753	2.1582	1.9916	3.1569	2.0746
	0.5	2.1846	3.3184	2.1997	2.0347	3.2000	2.1177

thickness ratio has a more significant impact on the frequency compared to the tapered ratio. This is because the plate's thickness directly affects its overall stiffness, and increasing the thickness makes the plate stiffer, leading to higher frequencies. Additionally, the impact of electrical loading meaningfully affects the plate's frequency. As the electrical loading changes from negative to positive values, the frequency shifts. The electric field applied to piezoelectric materials can either compress or stretch the plate, depending on whether the loading is negative or positive. The change in loading alters the stress distribution and the deformation of the plate, which, in turn, affects its natural frequency.

Figure 15 shows the assessment of PFGN Plate A with varying a/h, electrical loading, and different porosity distribution at

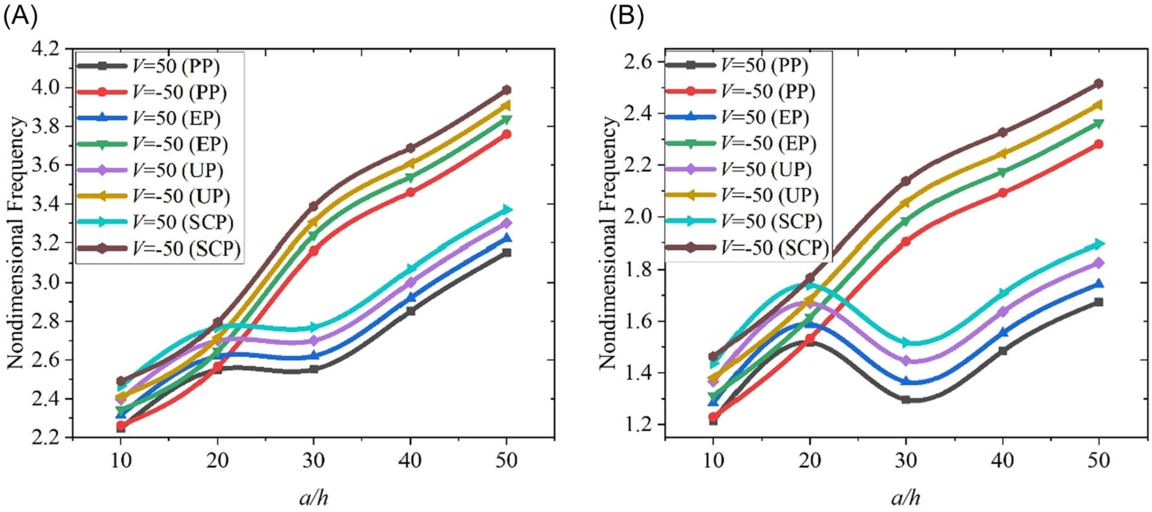

FIGURE 15 | Influence of the electrical loading with porosity distributions on the frequency of the PFGN Plate A at $k_w = 20$, $k_{px} = 20$, $k_{py} = 10$, $\Psi = 10$ (LF), $n_z = n_x = 2\Upsilon = 0.2$, and $\theta = 0°$: (A) CCCC, Plate A, (B) Case 1, Plate A.

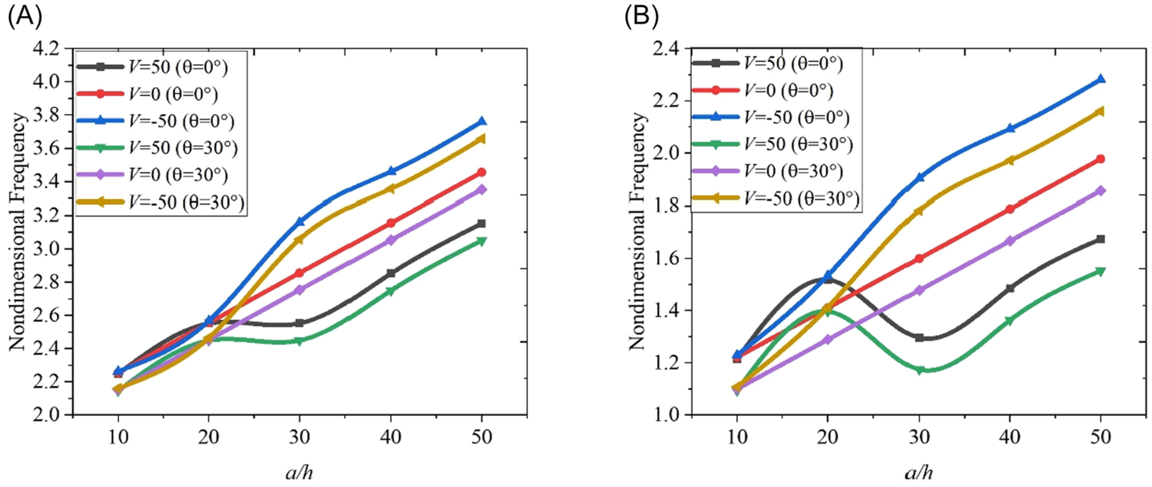

FIGURE 16 | Influence of the electrical loading with different orthotropic angles on the frequency of the perfect PFGN Plate A at $k_w = 20$, $k_{px} = 20$, $k_{py} = 10$, $\Psi = 10$ (LF), and $n_z = n_x = 2$: (A) CCCC, Plate A, (B) Case 1, Plate A.

$k_w = 20$, $k_{px} = 20$, $k_{py} = 10$, $\Psi = 10$ (LF), $n_z = n_x = 2$, $\Upsilon = 0.2$, and $\theta = 0°$. It is found that increasing the thickness ratio at a constant voltage raises the frequency. At a fixed thickness ratio, the frequency is influenced by the electrical voltages. Positive voltage values lead to a lower frequency, while negative values result in higher frequencies. This behavior is because electric voltage generates axial forces, and the nature of these axial forces depends on the sign of the electrical loading: positive means compressive and negative means tensile stress.

Figure 16 illustrates the impact of the electrical voltage with an orthotropic angle of the variable foundation on the frequency behavior of the PFGN Plate A at $k_w = 20$, $k_{px} = 20$, $k_{py} = 10$, $\Psi = 10$ (LF), and $n_z = n_x = 2$. The results show that for an initial thickness ratio of $a/h = 10$ to 20, the frequency variation of the plate is small. However, when the thickness is increased from 20 to 50, there is a sudden increment in the frequency because increasing the thickness enhances the plate's stiffness, which leads to higher frequencies.

Figure 17 displays the effect of the electrical loading and hygrothermal variation on the frequency response of the CCCC PFGN Plate A, with constant $n_z = n_x = 2$, $a/h = 20$ and $\theta = 0°$. It is seen that both positive and negative electrical loading significantly affect the frequency. In addition, the plate frequency is more dominantly affected by temperature change compared to moisture change. This is because temperature change lowers the plate's overall stiffness more effectively.

Figure 18 presents the effect of the tapered ratio, temperature change, and moisture change on the frequency response of CCCC MPFG Plate B at fixed parameters $n_z = n_x = 2$, $a/h = 20$, and $\theta = 0°$. Figure 18 shows that increases in the tapered ratio led to higher nondimensional frequencies in the absence of the orthotropic Pasternak foundation. Additionally, nonlinear hygrothermal loading results in higher nondimensional frequencies compared to uniform and linear hygrothermal loading. In the presence of hygrothermal loading, the stiffness of the MPFG plate decreases, leading to a reduction in the natural

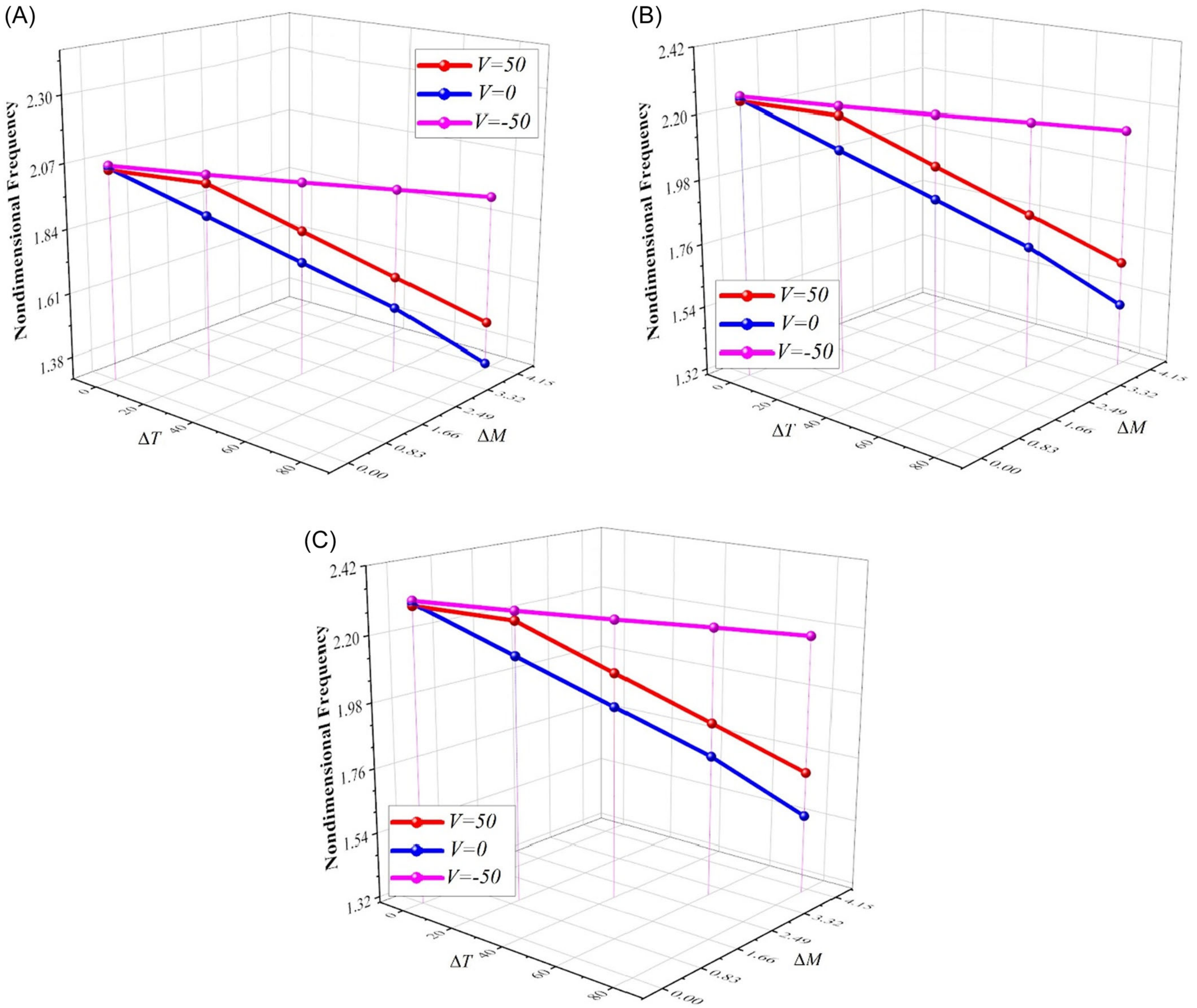

FIGURE 17 | Influence of the electrical loading with hygrothermal parameters on the perfect CCCC PFGN Plate A frequency, at $n_z = n_x = 2$, $a/h = 20$ and $\theta = 0°$: (A) CCCC, UHT, (B) CCCC, LHT, (C) CCCC, NHT.

frequencies. When the volume fraction of PZT-4 increases, the effective elastic modulus decreases, resulting in a decrease in frequency parameters. Similarly, an increase in the index value decreases the elastic modulus, leading to a reduction in natural frequency parameters.

6 | Conclusion

A numerical formulation is presented to investigate the nonlinear vibration behavior of the porous PFGN nonuniform plate with the orthotropic variable elastic foundations, subjected to the hygrothermoelectrical loading. The nonlinear governing equation is solved using a higher-order finite element technique coupled with a modified Newton-Raphson method. Parametric studies are conducted to determine the effect of various parameters on the frequency behavior of the PFGN porous plate. Based on the results and conclusions, the following key findings are observed:

- The distribution of porosity significantly impacts the frequency of the PFGN plate. Among all the porosity distributions, the SCP type has the most pronounced effect, surpassing the EP and UP types.
- Geometric nonuniformity in the PFGN plate always has a more significant impact on the frequency than in the uniform PFGN plate cases.
- Increasing the hygrothermal parameters, such as temperature and moisture change, reduces the mechanical characteristics of both plate structure and constituents, leading to a decrease in nondimensional frequency. The effect of moisture change on the frequency is less significant than the effect of temperature change. NHT-type hygrothermal loading has more substantial effect than LHT and UHT-type loading.
- The impact of the foundation parameters on the plate frequency is significant. As these parameters increase, their effect on the frequency becomes more pronounced. Among

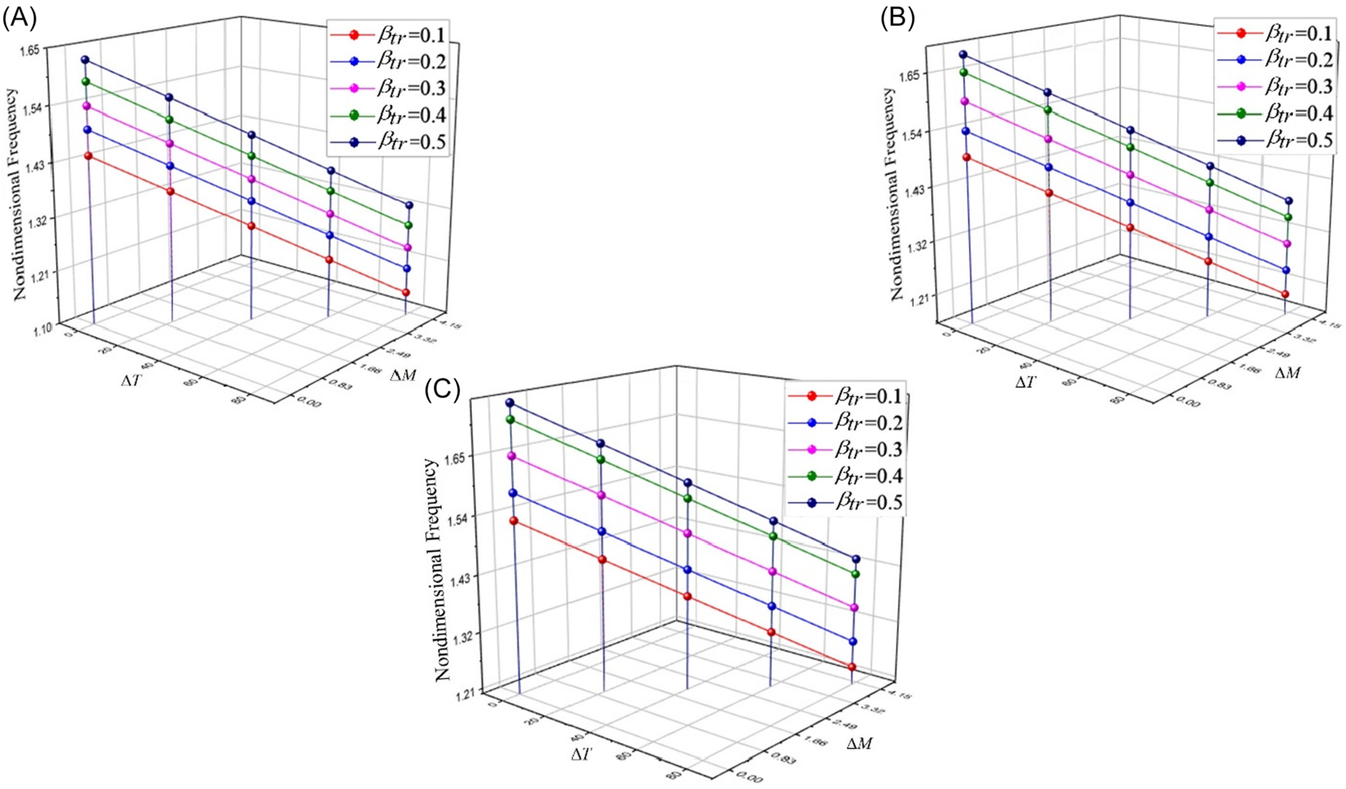

FIGURE 18 | Influence of the tapered ratio with hygrothermal parameters on the perfect CCCC MPFG Plate B frequency, at $n_z = n_x = 2$, $a/h = 20$, and $\theta = 0°$: (A) UHT, (B) LHT, (C) NHT.

all, parabolic-type variable foundations have a greater influence on the frequency compared to linear and sinusoidal types.

- The significant influence of the orthotropic angle and variable elastic foundations on the frequency response of PFGN plates is highlighted. The findings reveal that the frequency is directly influenced by the tapered ratio–an increase in the tapered ratio leads to an increase in the frequency. Conversely, the frequency is inversely related to the orthotropic angle, with a higher orthotropic angle resulting in a lower natural frequency.
- The multidirectional behavior of the PFGN plate is crucial for the accurate design of PFGN plate-based smart structures and devices under hygrothermoelectrical conditions. These findings are particularly relevant for applications, such as energy harvesting, vibration control, and structural health monitoring, where effective modeling and design are essential.
- This study highlights the adaptability of the proposed method in analyzing the interaction between different types of orthotropic variable elastic foundations, porosity, and various CSC and USC boundary conditions. The results demonstrate the effectiveness and flexibility of the approach in capturing the complex mechanical behavior of plates under different support and foundation configurations.

Acknowledgments

This study was supported by King Mongkut's University of Technology Thonburi's Postdoctoral Fellowship Under Research Project ID- 27929.

Conflicts of Interest

The authors declare no conflicts of interest.

Data Availability Statement

The raw/processed data essential to reproduce these findings cannot be shared at this time as the data also forms part of an ongoing study. Data will be presented on request.

References

1. W. P. Mason, “Piezoelectricity, its History and Applications,” *Journal of the Acoustical Society of America* 68, no. S1 (1980): S39.

2. S. Zhang, R. Xia, L. Lebrun, D. Anderson, and T. R. Shrout, “Piezoelectric Materials for High Power, High Temperature Applications,” *Materials Letters* 59, no. 27 (2005): 3471–3475.

3. T. Ikeda, *Fundamentals of Piezoelectricity* (Oxford University Press, 1996).

4. V. Birman and L. W. Byrd, “Modeling and Analysis of Functionally Graded Materials and Structures,” *Applied Mechanics Reviews* 60 (2007): 195–216.

5. C. C. Hong, “Thermal Vibration of Magnetostrictive Functionally Graded Material Shells by Considering the Varied Effects of Shear Correction Coefficient,” *International Journal of Mechanical Sciences* 85 (2014): 20–29.

6. P. Kumar and S. Harsha, “Response Analysis of Hybrid Functionally Graded Material Plate Subjected to Thermo-Electro-Mechanical Loading,” *Proceedings of the Institution of Mechanical Engineers, Part L: Journal of Materials: Design and Applications* 235, no. 4 (2021): 813–827.

7. A. M. A. Neves, A. J. M. Ferreira, E. Carrera, et al., “Static, Free Vibration and Buckling Analysis of Isotropic and Sandwich Functionally Graded Plates Using a Quasi-3D Higher-Order Shear Deformation

Theory and a Meshless Technique," *Composites, Part B: Engineering* 44, no. 1 (2013): 657–674.

8. W. Q. Chen and H. J. Ding, "On Free Vibration of a Functionally Graded Piezoelectric Rectangular Plate," *Acta Mechanica* 153, no. 3–4 (2002): 207–216.

9. K. Swaminathan, D. T. Naveenkumar, A. M. Zenkour, and E. Carrera, "Stress, Vibration and Buckling Analyses of FGM Plates—A State-of-the-Art Review," *Composite Structures* 120 (2015): 10–31.

10. Z. Su, G. Jin, and T. Ye, "Electromechanical Vibration Characteristics of Functionally Graded Piezoelectric Plates With General Boundary Conditions," *International Journal of Mechanical Sciences* 138–139 (2018): 42–53.

11. P. Kumar and S. P. Harsha, "Vibration Response Analysis of Exponential Functionally Graded Piezoelectric (EFGP) Plate Subjected to Thermo-Electro-Mechanical Load," *Composite Structures* 267 (2021): 113901.

12. Z. Zhong and E. T. Shang, "Three-Dimensional Exact Analysis of a Simply Supported Functionally Gradient Piezoelectric Plate," *International Journal of Solids and Structures* 40, no. 20 (2003): 5335–5352.

13. B. Uymaz and M. Aydogdu, "Three-Dimensional Vibration Analyses of Functionally Graded Plates Under Various Boundary Conditions," *Journal of Reinforced Plastics and Composites* 26, no. 18 (2007): 1847–1863.

14. X. L. Huang and H. S. Shen, "Nonlinear Vibration and Dynamic Response of Functionally Graded Plates in Thermal Environments," *International Journal of Solids and Structures* 41, no. 9–10 (2004): 2403–2427.

15. M. C. Manna, "Free Vibration of Tapered Isotropic Rectangular Plates," *Journal of Vibration and Control* 18, no. 1 (2012): 76–91.

16. B. Behjat and M. R. Khoshravan, "Geometrically Nonlinear Static and Free Vibration Analysis of Functionally Graded Piezoelectric Plates," *Composite Structures* 94, no. 3 (2012): 874–882.

17. P. M. Ramteke, N. Sharma, M. Dwivedi, S. K. Das, C. R. Uttarwar, and S. K. Panda, "Theoretical Thermoelastic Frequency Prediction of Multi (Uni/Bi) Directional Graded Porous Panels and Experimental Verification," *Structures* 54 (2023): 618–630.

18. P. Kumar and S. P. Harsha, "Electroelastic Static and Vibration Response Analysis of Sigmoid PZT-5A/Pt-Based Smart Functionally Graded Plate," *International Journal of Structural Stability and Dynamics* 22, no. 14 (2022): 2250155.

19. H. J. Xiang and Z. F. Shi, "Static Analysis for Functionally Graded Piezoelectric Actuators or Sensors Under a Combined Electro-Thermal Load," *European Journal of Mechanics-A/Solids* 28, no. 2 (2009): 338–346.

20. A. Komeili, A. H. Akbarzadeh, A. Doroushi, and M. R. Eslami, "Static Analysis of Functionally Graded Piezoelectric Beams Under Thermo-Electro-Mechanical Loads," *Advances in Mechanical Engineering* 3 (2011): 153731.

21. M. R. Barati and A. M. Zenkour, "Electro-Thermoelastic Vibration of Plates Made of Porous Functionally Graded Piezoelectric Materials Under Various Boundary Conditions," *Journal of Vibration and Control* 24, no. 10 (2018): 1910–1926.

22. P. Kumar and S. P. Harsha, "Vibration Response Analysis of Sigmoidal Functionally Graded Piezoelectric (FGP) Porous Plate Under Thermo-Electric Environment," *Mechanics Based Design of Structures and Machines* 58, no. 8 (2021): 4604–4634, https://doi.org/10.1080/15397734.2021.1971090.

23. P. Kumar and A. Harsha, "Vibration Response Analysis of the Bi-Directional Porous Functionally Graded Piezoelectric (BD-FGP) Plate," *Mechanics Based Design of Structures and Machines* 52, no. 1 (2024): 126–151, https://doi.org/10.1080/15397734.2022.2099418.

24. P. Kumar and S. P. Harsha, "Dynamic Analysis of Porosity Dependent Functionally Graded Sigmoid Piezoelectric (FGSP) Plate," *Structures* 46 (2022): 1737–1752.

25. V. Kumar, S. J. Singh, and S. P. Harsha, "Temperature-Dependent Vibration Characteristics of Porous FG Material Plates Utilizing FSDT," *International Journal of Structural Stability and Dynamics* 24, no. 7 (2023): 2450072.

26. M. Şimşek, "Bi-Directional Functionally Graded Materials (BDFGMs) for Free and Forced Vibration of Timoshenko Beams With Various Boundary Conditions," *Composite Structures* 133 (2015): 968–978.

27. C. F. Lü, C. W. Lim, and W. Q. Chen, "Exact Solutions for Free Vibrations of Functionally Graded Thick Plates on Elastic Foundations," *Mechanics of Advanced Materials and Structures* 16, no. 8 (2009): 576–584.

28. D. Chen, J. Yang, and S. Kitipornchai, "Elastic Buckling and Static Bending of Shear Deformable Functionally Graded Porous Beam," *Composite Structures* 133 (2015): 54–61.

29. P. Van Vinh, M. Avcar, M. O. Belarbi, and A. Tounsi, "A New Higher-Order Mixed Four-Node Quadrilateral Finite Element for Static Bending Analysis of Functionally Graded Plates," *Structures* 47 (2023): 1595–1612.

30. Z. Nan, Z. Xie, Z. Shijie, and C. Dejin, "Size-Dependent Static Bending and Free Vibration Analysis of Porous Functionally Graded Piezoelectric Nanobeams," *Smart Materials and Structures* 29, no. 4 (2020): 045025.

31. X. Zhao, S. Zheng, and Z. Li, "Effects of Porosity and Flexoelectricity on Static Bending and Free Vibration of AFG Piezoelectric Nanobeams," *Thin-Walled Structures* 151 (2020): 106754.

32. A. Behravan Rad, "Static Analysis of Nonuniform 2D Functionally Graded Auxetic-Porous Circular Plates Interacting With the Gradient Elastic Foundations Involving Friction Force," *Aerospace Science and Technology* 76 (2018): 315–339.

33. S. Li, S. Zheng, and D. Chen, "Porosity-Dependent Isogeometric Analysis of Bi-Directional Functionally Graded Plates," *Thin-Walled Structures* 156 (2020): 106999.

34. E. Carrera, S. Brischetto, and P. Nali, *Plates and Shells for Smart Structures: Classical and Advanced Theories for Modeling and Analysis* (John Wiley & Sons, 2011). 36.

35. I. M. Mudhaffar, A. Tounsi, A. Chikh, M. A. Al-Osta, M. M. Al-Zahrani, and S. U. Al-Dulaijan, "Hygro-Thermo-Mechanical Bending Behavior of Advanced Functionally Graded Ceramic Metal Plate Resting on a Viscoelastic Foundation," *Structures* 33 (2021): 2177–2189.

36. A. Prakash, P. Kumar, V. H. Saran, and S. P. Harsha, "NURBS Based Thermoelastic Behaviour of Thin Functionally Graded Sigmoidal (TFGS) Porous Plate Resting on Variable Winkler's Foundation," *International Journal of Mechanics and Materials in Design* 19, no. 4 (2023): 831–860, https://doi.org/10.1007/s10999-023-09654-9.

37. P. Kumar and S. P. Harsha, "Thermoelectric Nonlinear Vibration and Buckling Analysis of the Smart Porous Core Sandwich Plate (SPCSP) Resting on the Elastic Foundation," *Journal of Intelligent Material Systems and Structures* 34 (2023): 1587–1616, https://doi.org/10.1177/1045389X221142085.

38. P. Kumar and S. P. Harsha, "Static Analysis of Porous Core Functionally Graded Piezoelectric (PCFGP) Sandwich Plate Resting on the Winkler/Pasternak/Kerr Foundation Under Thermo-Electric Effect," *Materials Today Communications* 32 (2022): 103929.

39. F. Tornabene, "Free Vibration Analysis of Functionally Graded Conical, Cylindrical Shell and Annular Plate Structures With a Four-Parameter Power-Law Distribution," *Computer Methods in Applied Mechanics and Engineering* 198, no. 37–40 (2009): 2911–2935.

40. M. Y. Tharwan, et al., "Size-Dependent Buckling of Multidirectional Porous Metal Foam Nanoshells Resting on an Orthotropic Elastic

Foundation," *Archives of Civil and Mechanical Engineering* 25, no. 1 (2025): 1–22.

41. A. Kutlu, B. Uğurlu, M. H. Omurtag, and A. Ergin, "Dynamic Response of Mindlin Plates Resting on Arbitrarily Orthotropic Pasternak Foundation and Partially in Contact With Fluid," *Ocean Engineering* 42 (2012): 112–125.

42. A. G. Arani, Z. K. Maraghi, and H. K. Arani, "Orthotropic Patterns of Pasternak Foundation in Smart Vibration Analysis of Magnetostrictive Nanoplate," *Proceedings of the Institution of Mechanical Engineers, Part C: Journal of Mechanical Engineering Science* 230, no. 4 (2016): 559–572.

43. M. Sharif Zarei, M. H. Hajmohammad, M. Mostafavifar, and M. Mohammadimehr, "Influence of Temperature Change and Humidity Condition on Free Vibration Analysis of a Nano Composite Sandwich Plate Resting on Orthotropic Pasternak Foundation by Considering Agglomeration Effect," *Journal of Sandwich Structures & Materials* (2017): 1099636217735118, https://doi.org/10.1177/1099636217735118.

44. M. Ermis, A. Kutlu, N. Eratlı, and M. H. Omurtag, "Free Vibration of Axially FG Curved Beam on Orthotropic Pasternak Foundation via Mixed FEM," *Journal of the Brazilian Society of Mechanical Sciences and Engineering* 44, no. 12 (2022): 597.

45. D. Li, Z. Deng, and G. Chen, "Free Vibration of Functionally Graded Sandwich Plates in Thermal Environments," *International Journal of Mechanical System Dynamics* 3, no. 1 (2023): 39–47.

46. B. Karami, M. H. Ghayesh, S. Hussain, and M. Amabili, "On the Size-Dependent Vibrations of Doubly Curved Porous Shear Deformable FGM Microshells," *International Journal of Mechanical System Dynamics* 4 (2024): 387–405, https://doi.org/10.1002/msd2.12137.

47. M. Eghbali and S. A. Hosseini, "A Complex Solution on the Dynamic Response of Sandwich Graphene-Reinforced Aluminum-Based Composite Beams With Copper Face Sheets Under Two Moving Constant Loads on an Elastic Foundation," *International Journal of Mechanical System Dynamics* 3, no. 3 (2023): 251–264.

48. A. Harsha and P. Kumar, "Impact of the Porosity and Elastic Foundation on Frequency and Buckling Response of Bidirectional Functionally Graded Piezoelectric Porous Plate," *International Journal of Structural Stability and Dynamics* 24, no. 7 (2024): 2450077.

49. A. Harsha and P. Kumar, "Thermoelectric Elastic Analysis of Bi-Directional Three-Layer Functionally Graded Porous Piezoelectric (FGPP) Plate Resting on Elastic Foundation," *Forces in Mechanics* 8 (2022): 100112.

50. E. Salari, S. A. S. Vanini, and A. Ashoori, "Nonlinear Thermal Stability and Snap-Through Buckling of Temperature-Dependent Geometrically Imperfect Graded Nanobeams on Nonlinear Elastic Foundation," *Materials Research Express* 6, no. 12 (2020): 1250j6.

51. P. Kumar and S. P. Harsha, "Static, Buckling and Vibration Response Analysis of Three-Layered Functionally Graded Piezoelectric Plate Under Thermo-Electric Mechanical Environment," *Journal of Vibration Engineering & Technologies* 10, no. 4 (2022): 1561–1598.

52. P. Kumar and S. P. Harsha, "Static and Vibration Response Analysis of Sigmoid Function-Based Functionally Graded Piezoelectric Non-Uniform Porous Plate," *Journal of Intelligent Material Systems and Structures* 33, no. 17 (2022): 2197–2227.

53. E. Salari and S. A. Sadough Vanini, "Nonlocal Nonlinear Static/Dynamic Snap-Through Buckling and Vibration of Thermally Post-Buckled Imperfect Functionally Graded Circular Nanoplates," *Wavesin Random and Complex Media* 35, no. 2 (2025): 3805–3851, https://doi.org/10.1080/17455030.2022.2055810.

54. E. Salari and S. A. Sadough Vanini, "Small/Large Amplitude Vibration, Snap-Through and Nonlinear Thermo-Mechanical Instability of Temperature-Dependent FG Porous Circular Nanoplates," *Engineering With Computers* 39, no. 3 (2023): 2295–2326.

55. A. R. Ashoori, S. A. S. Vanini, and E. Salari, "Size-Dependent Axisymmetric Vibration of Functionally Graded Circular Plates in Bifurcation/Limit Point Instability," *Applied Physics A* 123 (2017): 226.

56. P. Kumar and S. P. Harsha, "Vibration Response Analysis of PZT-4/PZT-5H Based Functionally Graded Tapered Plate Subjected to Electro-Mechanical Loading," *Mechanics Research Communications* 116 (2021): 103765.

57. P. Kumar and S. P. Harsha, "Response Analysis of Functionally Graded Piezoelectric Plate Resting on Elastic Foundation Under Thermo-Electro Environment," *Journal of Composite Materials* 56, no. 24 (2022): 3749–3767.

58. P. Kumar and S. P. Harsha, "Static and Vibration Response Analysis of PZT-5A/PT Based Smart Functionally Graded (SFG) Plate Subjected to Electromechanical Loading." *International Conference on Vibration Engineering and Technology of Machinery* (Springer Nature, 2021), 1–12, https://doi.org/10.1007/978-981-99-4721-8_37.

59. M. Ghadiri, F. Ebrahimi, E. Salari, S. A. H. Hosseini, and G. R. Shaghaghi, "Electro-Thermo-Mechanical Vibration Analysis of Embedded Single-Walled Boron Nitride Nanotubes Based on Nonlocal Third-Order Beam Theory," *International Journal for Multiscale Computational Engineering* 13, no. 5 (2015): 443–461.

60. E. Salari, A. R. Ashoori, S. A. Sadough Vanini, and A. H. Akbarzadeh, "Nonlinear Dynamic Buckling and Vibration of Thermally Post-Buckled Temperature-Dependent FG Porous Nanobeams Based on the Nonlocal Theory," *Physica Scripta* 97, no. 8 (2022): 085216.

61. F. Ebrahimi and E. Salari, "Analytical Modeling of Dynamic Behavior of Piezo-Thermo-Electrically Affected Sigmoid and Power-Law Graded Nanoscale Beams," *Applied Physics A* 122, no. 9 (2016): 793.

62. F. Ebrahimi and E. Salari, "Semi-Analytical Vibration Analysis of Functionally Graded Size-Dependent Nanobeams With Various Boundary Conditions," *Smart Structures and Systems* 19, no. 3 (2017): 243–257.

63. F. Ebrahimi and E. Salari, "Effect of Non-Uniform Temperature Distributions on Nonlocal Vibration and Buckling of Inhomogeneous Size-Dependent Beams," *Advances in Nano Research* 6, no. 4 (2018): 377–397, https://doi.org/10.12989/ANR.2018.6.4.377.

64. P. Kumar and S. P. Harsha, "Hygrothermal Static Bending and Deflection Responses of Porous Multidirectional Nanofunctionally Graded Piezoelectric (NFGP) Plates With Variable Thickness on Elastic Foundations," *International Journal of Mechanical System Dynamics* 5 (2025): 40–66, https://doi.org/10.1002/msd2.70003.

65. P. Kumar and S. P. Harsha, "Modal Analysis of Functionally Graded Piezoelectric Material Plates," *Materials Today: Proceedings* 28 (2020): 1481–1486.

66. H. Ezzati, F. Ebrahimi, and E. Salari, "Exploring Graphene Origami-Enabled Metamaterials: A Review," *Journal of Computational Applied Mechanics* 56, no. 1 (2025): 249–263.

67. F. Ghasemi, E. Salari, A. H. Zamanian, and A. Rastgoo, "Experimental Mechanical Properties, Nonlinear Bending and Instability Analysis of 3D-Printed Auxetic Tubular Metastructures Using Multiscale Finite Element and Ritz Methods," *Mechanics of Advanced Materials and Structures* (2024): 1–24, https://doi.org/10.1080/15376494.2024.2436650.

68. F. Ghasemi, E. Salari, A. Salari, A. Rastgoo, D. Li, and J. Deng, "Integrating Analytical and Machine Learning Methods for Investigating Nonlinear Bending and Post-Buckling Behavior of 3D-Printed Auxetic Tubes," *Engineering With Computers* (2024), https://doi.org/10.1007/s00366-024-02091-y.

69. A. R. Ashoori, E. Salari, and S. A. Sadough Vanini, "A Thermo-Electro-Mechanical Vibration Analysis of Size-Dependent Functionally Graded Piezoelectric Nanobeams." *Advances in High Temperature Ceramic Matrix Composites and Materials for Sustainable Development* (Ceramic Transactions, 2017), 547–558. Volume CCLXIII, https://doi.org/10.1002/9781119407270.ch49.

70. F. Ebrahimi, G. R. Shaghaghi, and E. Salari, "Vibration Analysis of Size-Dependent Nano Beams Based on Nonlocal Timoshenko Beam Theory," *Journal of Mechanical Engineering and Technology (JMET* 6, no. 2 (2014): 1–13, https://jmet.utem.edu.my/jmet/article/view/340/220.

71. F. Ghasemi, E. Salari, A. Rastgoo, D. Li, and J. Deng, "Nonlinear Vibration Analysis of Pre/Post-Buckled 3D-Printed Tubular Metastructures," *Engineering Analysis With Boundary Elements* 165 (2024): 105777.

72. M. R. Nasri, E. Salari, A. Salari, and S. A. Sadough Vanini, "Nonlinear Bending and Buckling Analysis of 3D-Printed Meta-Sandwich Curved Beam With Auxetic Honeycomb Core," *Aerospace Science and Technology* 152 (2024): 109339.

73. J. Yang, *An Introduction to the Theory of Piezoelectricity* (Springer, 2005). 9.

74. J. N. Reddy, *Theory and Analysis of Elastic Plates and Shells* (CRC Press, 1999). 2nd ed.

75. G. C. Sih, J. G. Michopoulos and S. C. Chou, ed., *Hygrothermoelasticity* (Springer Science & Business Media, 1986).

76. T. Amornsawaddirak and S. Aimmanee, "A Symplectic Analytical Approach for Beams Resting on Multi-Layered Elastic Foundations," *International Journal of Mechanical Sciences* 153–154 (2019): 457–469.

77. K. J. Bathe, *Finite Element Procedures* (Prentice Hall, 2006).

78. P. G. Bergan and R. W. Clough, "Convergence Criteria for Iterative Processes," *AIAA Journal* 10, no. 8 (1972): 1107–1108.

79. M. Amabili, *Nonlinear Vibrations and Stability of Shells and Plates* (Cambridge University Press, 2008).

Appendix

The shape function derivates appearing in Equations (13–15) can be written as

$$\left.\begin{aligned}
&[\boldsymbol{B}_1] = \begin{bmatrix} \frac{\partial}{\partial x} & 0 & 0 \\ 0 & \frac{\partial}{\partial x} & 0 \\ \frac{\partial}{\partial x} & \frac{\partial}{\partial x} & 0 \end{bmatrix}; [\boldsymbol{B}_2] = \begin{bmatrix} \frac{\partial}{\partial x} & 0 \\ 0 & \frac{\partial}{\partial x} \\ \frac{\partial}{\partial x} & \frac{\partial}{\partial x} \end{bmatrix}; [\boldsymbol{B}_5] = \begin{bmatrix} 0 & 0 & \frac{\partial}{\partial x} \\ 0 & 0 & \frac{\partial}{\partial y} \end{bmatrix}; [\boldsymbol{B}_6] = \begin{bmatrix} 1 & 0 \\ 0 & 1 \end{bmatrix}; [\boldsymbol{z}_1] = \begin{bmatrix} z & 0 & 0 \\ 0 & z & 0 \\ 0 & 0 & 2z \end{bmatrix}; \\
&[\boldsymbol{B}_{\Theta i}] = [\boldsymbol{L}_{\Theta}][\boldsymbol{N}_{\Theta i}] = \begin{bmatrix} \frac{\partial}{\partial x} \\ \frac{\partial}{\partial y} \\ \frac{\partial}{\partial z} \end{bmatrix}[\boldsymbol{N}_{\Theta i}]; [\boldsymbol{B}_4] = \begin{bmatrix} 0 & 0 & \frac{\partial}{\partial x} \\ 0 & 0 & \frac{\partial}{\partial y} \\ 0 & 0 & 0 \end{bmatrix}; [\boldsymbol{B}_3] = \begin{bmatrix} \frac{\partial w_0}{\partial x} & 0 & 0 \\ 0 & \frac{\partial w_0}{\partial x} & 0 \\ \frac{\partial w_0}{\partial x} & \frac{\partial w_0}{\partial x} & 0 \end{bmatrix}; [\boldsymbol{z}_3] = \begin{bmatrix} 1 & 0 \\ 0 & 1 \end{bmatrix}
\end{aligned}\right\}. \tag{A.1}$$